Meridional transport of physical and biogeochemical tracers by Southern Ocean eddies

Ramkrushnbhai S. Patel[1,2], Andrew Lenton[3], Helen E. Phillips[1,4,5], Peter G. Strutton[1,2], Tyler Rohr[1,3,4], Joan Llort[6], Matthew A. Chamberlain[3]

[1]Institute for Marine and Antarctic Studies, University of Tasmania, Hobart, Tasmania, Australia
[2]Australian Research Council Centre of Excellence for Climate Extremes, University of Tasmania, Hobart, Tasmania, Australia
[3]Commonwealth Scientific and Industrial Research Organisation (CSIRO), Environment, Castray Esplanade, Hobart, Tasmania, Australia
[4]Australian Antarctic Program Partnership, Institute for Marine and Antarctic Studies, University of Tasmania, Hobart, Tasmania, Australia
[5]Australian Centre for Excellence in Antarctic Science, Hobart, Tasmania, Australia
[6]Barcelona Supercomputing center, Barcelona, Spain

Key Points:

- Standing meanders in the Antarctic Circumpolar Current are hotspots for poleward heat and salt, as well as equatorward nitrate transport.
- Long-lived cyclonic eddies contribute less than 20% of the poleward transient heat and equatorward nitrate transport across the Subantarctic Front south of Tasmania.
- Integrated Surface Elevation emerges as a promising proxy for estimating the transport of physical and biogeochemical tracers by coherent eddies.

Corresponding author: Ramkrushnbhai S. Patel, Ramkrushnbhai.Patel@utas.edu.au

Abstract

Meridional eddy transport across the Antarctic Circumpolar Current is an essential component of the global meridional overturning circulation and the transport of climate relevant tracers. Challenges in comparing model and observational estimates of the transport arise from varying methodologies describing 'eddy' processes. We reconcile the approach used in shipboard surveys of eddies, complemented by satellite eddy tracking, with Reynolds decomposition applied to model outputs. This allows us to estimate the fraction of total meridional tracer transport attributed to coherent eddies in a global 0.1° ocean model. The model realistically simulates observed eddy kinetic energy and three-dimensional characteristics, particularly in representing an observed cyclonic eddy near 150 °E, a hotspot for poleward heat flux. Annual meridional transports due to coherent eddies crossing the Subantarctic Front are estimated by vertically and radially integrating the tracer contents of all eddies. Notably, only cyclonic eddies moving equatorward across the Subantarctic Front contribute to the coherent eddy transport, with no anticyclonic eddies found to cross the front poleward in this region. Applying Reynolds decomposition, our study reveals predominantly poleward meridional transports due to all transient processes in a standing meander, particularly between the northern and southern branches of the Subantarctic Front. Coherent, long-lived eddies tracked from satellite data contribute less than 20% to transient poleward heat transport, and equatorward nitrate transport in the model. Furthermore, we demonstrate that the integrated surface elevation of mesoscale eddies serves as a reliable proxy for inferring subsurface eddy content.

Plain Language Summary

The Antarctic Circumpolar Current regulates how much heat, salt, and nutrients can be transported across it. Ocean swirls, known as eddies, are vital for this transport, influencing the large-scale circulation of the Southern Ocean and supplying essential oxygen and nutrients to subtropical and tropical waters. But, comparing the eddy transports from shipboard observations and ocean models has been challenging due to different methods used to define eddies. This makes it difficult to know if observations and models agree. In this paper, we apply methods used for observations to a model so that we can directly compare the model and observations. We focussed on the Subantarctic Front of the Antarctic Circumpolar Current in a region of intense eddy heat transport

toward Antarctica. We showed that the transport by coherent eddies, which ship observations can measure, agreed between the model and observations. We further showed that this part of the transport only accounted for 20% of the total eddy transport by all other transient processes such as smaller eddies, filaments, and waves. This suggests that high resolution models validated by shipboard observations are essential for accurately quantifying the transport of heat and salt toward Antarctica and nutrients toward the equator. Additionally, we have shown that the volume of water displaced by an eddy at the ocean's surface can tell us about how much heat, salt, and nutrients it carries.

1 Introduction

The poleward transport of heat and salt in the Southern Ocean is a key component of the meridional overturning circulation and is essential to maintaining the Earth's energy balance. The transport of nutrients, particularly nitrate, from the Southern Ocean to lower latitudes via subduction of Subantarctic Mode Water shapes the global nutrient budget and lower latitude primary productivity (Palter et al., 2010). The relative importance of the mechanisms that transport heat, salt, and nutrients (referred to here as tracers) across the quasi-zonal, eastward-flowing Antarctic Circumpolar Current (ACC) remains an active area of research.

Mesoscale eddy processes play a dominant role in the transport of tracers. However, the term "eddy" has been used interchangeably in the literature for either coherent ring structures or fluctuations about an Eulerian time or spatial mean state or both. This interchangeability of the eddy term has divided studies of the poleward transport of tracers into two research avenues: meridional transport by isolated ring structures, referred to as coherent eddies, and transport by the covariance of velocity and tracer fluctuations, which we refer to as transient processes. The former research primarily developed from ship-based observations of coherent mesoscale eddies (e.g. TheRingGroup, 1981; Joyce et al., 1981; Morrow et al., 2004; Patel et al., 2019, 2020) and the latter developed from time-series analysis of moored observations and eddy-resolving ocean circulation models (e.g. Phillips & Rintoul, 2000; Meijers et al., 2007; Watts et al., 2016; Tréguier et al., 2014; Sekma et al., 2013; Tréguier et al., 2017). These different avenues have the potential to confuse comparisons between studies, as coherent eddies are transient features, but not all transient processes are coherent eddies. If reconciled, these two avenues present an opportunity to better understand the role of coherent mesoscale eddies in the

poleward transport of heat, salt, and nitrate, as well as what types of observations and models may be required to understand and project future changes.

Transient eddy processes are typically defined as the covariance of velocity and tracer fluctuations, commonly known as Reynolds fluxes. They encompass mesoscale eddies, filaments, and submesoscale processes occurring along fronts and at the edges of eddies. These processes work collectively by stirring tracers across meridional gradients to achieve the poleward transport of heat and salt, and contribute to the equatorward transport of nutrients (Jayne & Marotzke, 2002; Thompson & Naveira Garabato, 2014; Su et al., 2018; Abernathey & Haller, 2018; Patel et al., 2019, 2020). Most of this poleward transport occurs at specific locations where the Antarctic Circumpolar Current (ACC) interacts with bathymetry, generating standing meanders in the ACC and enhanced eddy activity (Naveira Garabato et al., 2011; Thompson & Sallée, 2012; Dufour et al., 2015; Foppert et al., 2017). By understanding the relative importance of the different types of transient processes, it becomes possible to investigate the sensitivity of tracer transport to changes in the climate system. Furthermore, better parameterisation of mesoscale phenomena in climate models that do not resolve these processes can lead to improved climate model projections.

Coherent mesoscale eddies are typically defined as rotating water bodies of $\mathcal{O}$(10-100) km diameter with a lifespan of at least 30 days to years, extending from the surface down to $\mathcal{O}$(100) m (Chelton et al., 2011; Petersen et al., 2013; Frenger et al., 2015). They laterally transport oceanic properties by trapping tracers in their core and traversing the ocean, stirring tracers gradient locally, or performing both actions simultaneously (McGillicuddy Jr, 2016, and references therein). In the Southern Ocean, these mesoscale eddies are generated mainly due to the conversion of the available potential energy of the steeply sloping isopycnals into eddy kinetic energy via baroclinic instabilities (Rintoul, 2018). This baroclinic instability is enhanced where the ACC interacts with oceanic ridges, for instance, south of Tasmania where the ACC encounters the Southeast Indian Ridge (SEIR Naveira Garabato et al., 2011; Thompson & Sallée, 2012).

Given the abundance and mobility of eddies, it is difficult to obtain three-dimensional observations of their population. The approach taken in ship-based studies is to use a satellite proxy to extrapolate the results from a hydrographic survey to larger spatial and temporal scales. For example, Swart et al. (2008) used an empirical relationship between

the Integrated Surface Elevation (ISE) of an eddy estimated from sea surface height anomalies together with the available heat anomaly of the eddy measured from the ship to quantify the changing heat content of the eddy through time. Likewise, Patel et al. (2019, 2020) used a relationship between ISE and available heat, salt and nitrate anomalies to estimate the meridional transport by eddies at a hotspot of poleward heat transport across the ACC. Notably, these proxies are grounded in single hydrographic surveys, and lack generalisation.

Using satellite altimetry observations, Foppert et al. (2017) demonstrated that the standard deviation of sea surface height can be used as a proxy for the time-mean depth-integrated divergent transient heat flux across the Southern Ocean. Comparing estimates of the total meridional transient heat flux from this satellite proxy with transport by discrete eddies from ship-based observations, Patel et al. (2019) estimated that long-lived cyclonic eddies transport about 20% of the total transient poleward heat flux across the Subantarctic Front near 150°E. These results present a tantalising first observation-based estimate of the relative contribution of coherent eddies to the total transient transport of heat. However, the strong reliance on proxies for coherent eddy transport (Patel et al., 2019) and the total transient heat transport (Foppert et al., 2017) can lead to large uncertainty in the estimates. Moreover, as of now, there exists no comparable estimate for biogeochemical tracers.

Our objective is to directly quantify the relative importance of coherent eddies in the total meridional transport by all transient processes and to assess the reliability of the ISE-proxy in a hotspot for eddy heat transport south of Tasmania, using outputs from an eddy-resolving ocean model. To this end, we first evaluate the model's performance in representing both the surface and subsurface structure of coherent eddies compared with satellite and shipboard observations, respectively (Section 4). Next, we quantify the proportion of coherent mesoscale eddies in the meridional transport of tracers by the total transient processes (Section 5). Finally, we demonstrate that ISE-proxy constrained by *in situ* observations, can reliably infer transport from satellite observations (Section 6).

2 Data

2.1 Model outputs

We used the outputs from a historical simulation of the Ocean Forecasting Australia Model, version 3, forced with Japanese 55-year Reanalysis (OFAM3-JRA55). OFAM3-JRA55 is based on the Geophysical Fluid Dynamics Laboratory's Modular Ocean Model, version 4p1 (Griffies et al., 2009) and is coupled to the Whole Ocean Model of Biogeochemistry And Trophic dynamics (WOMBAT). WOMBAT is a biogeochemical model with a single class of phytoplankton and zooplankton computed on the same grid as temperature (Oke et al., 2013). WOMBAT only explicitly resolves the phosphate cycle, linking nitrate, carbon, and oxygen using fixed stoichiometry of 16:106:-172:1 (N:C:O_2:P; Sarmiento, 2013).

The historical experiment has a "mesoscale eddy-rich" spatial resolution of 0.1° for all longitudes and between 75°S and 75°N. The nominal resolution of 0.1° resolves mesoscale eddies, or the first baroclinic deformation radius, in our Southern Ocean study region (Hallberg, 2013; Griffies, 2014). The model extends to a depth of 5000 m with 51 non-uniform vertical z* levels (geopotential levels that scale with the free surface). There are 14 layers between the surface and 100 m and 12 layers below 1000 m, giving a 5 m resolution near the sea surface and approximately 1000 m near the sea floor.

In this study, we used the last 8 years of the historical simulation for the following variables: daily averaged sea surface height, and daily averaged three-dimensional temperature, salinity, nitrate, and horizontal velocity components. The length of the study period is informed by the literature. A common practice in similar studies is to select the last 8 to 10 years of a model simulation, as they are more likely to be free from model instabilities and drift (e.g Meijers et al., 2007; Tréguier et al., 2014; Buzzicotti et al., 2023). Furthermore, we assess the sensitivity of the averaging period to the time-mean transient tracer transport (Section 3.4).

The details of the OFAM3-JRA55 setup and its extensive validation can be found in Zhang et al. (2016). The simulation exhibits warm biases in the ACC (Zhang et al., 2016). The volume transport of the ACC in the model is about 10 to 15% stronger than observed estimates in the Drake Passage and south of Tasmania, as shown in Oke et al.

(2013, Fig. 7a and Table 2). In addition, we validate the representation of the Southern Ocean eddy field in our study region (Section 4).

2.2 Satellite data

To validate the surface signature of transient processes in the model, we used multi-mission daily delayed-time gridded sea surface heights, geostrophic velocity and absolute dynamic topography from satellite altimetry over the period overlapping with the model output (2007-2014). These measurements are available on a Cartesian 0.25° grid at daily temporal resolution from Copernicus Marine Environment Monitoring Services, `https://resources.marine.copernicus.eu/?option=com_csw&task=results` and the data processing is described at `https://duacs.cls.fr/`.

2.3 Hydrographic data

Hydrographic observations from Voyage IN2016_V02 of *RV Investigator* were used to validate the vertical structure of eddies in the model. This voyage took place from March to April 2016 in a standing meander of the Subantarctic Front (SAF) upstream of Macquarie Ridge, near 52°S, 142°E. We used eleven conductivity-temperature-depth (CTD) profiles of the upper 1500 m to construct a vertical transect across the full diameter of a cyclonic eddy. The watermass structure, velocity field and time-varying surface characteristics of the sampled eddy are described in Patel et al. (2019). Biogeochemical properties and meridional transport by this eddy are described in Patel et al. (2020). Each CTD profile recorded temperature, salinity, pressure, fluorescence, and backscatter. Bottle samples were taken at 24 depths to measure the concentration of nutrients: nitrate, nitrite, silicate, phosphate, ammonia, chlorophyll-A, and particulate organic carbon.

3 Methods

3.1 Identification of the fronts

We determined the time-varying ACC front locations by applying the hybrid-dynamic criteria to the OFAM simulation as prescribed in Langlais et al. (2011). This approach combines hydrography, transport maxima and sea surface height to define frontal positions. In the model, the sea surface height contours of -0.4, -1, -1.4 m were selected by the method to represent the northern and southern branches of the Subantarctic Front

and Polar Front south of Tasmania, respectively. For satellite data, we used absolute dynamic height contours of 0.2, -0.4, -1.0 m to mark the northern and southern branches of the Subantarctic Front and Polar Front, respectively after Moreau et al. (2017); Patel et al. (2019, 2020). Further details about frontal variability, comparison of the front position between ocean general circulation models and observations, and sensitivity to various frontal identification methods are discussed in detail in Langlais et al. (2010, 2011).

3.2 Eddy detection and tracking

The identification and tracking of eddies was performed using software developed by Faghmous et al. (2015). The software was applied to both the historical simulation and satellite altimetry data for the study period. An eddy is identified at each time step as a single extremum enveloped in a closed contour of sea surface height anomaly. This extremum is a local minimum for cyclonic eddies and a local maximum for anticyclonic eddies. The extremum is defined by comparing each grid point with its surrounding grid points. For modelled sea surface height anomaly (0.1°), each grid point is compared to 100 surrounding grid points. For the lower spatial resolution (0.25°) altimetry sea surface height, 16 surrounding grid points are used, covering the same area as 100 model grid points. We have tested the sensitivity to the search window in the model for 3 cases: 16, 49 and 100 grid points. We found that using the same window as observations (4×4, 16 grid points) identifies too many small eddies in the model. For all cases, model, and altimetry agree well, as summarised in Table S1 and S2.

During the tracking, we allowed an eddy to disappear for one day without terminating the track. To remove very short-lived eddies and other features that could be tracked by the software, we filtered the results based on lifespan criterion (lifespan $\geq$ 30 days), as suggested by Faghmous et al. (2015). In this study, we focus on eddies that persisted for at least 90 days – referred to as long-lived eddies. The amplitude of an eddy is computed as the difference in magnitude between the extremum value of sea surface height anomaly at the centre and the height of the eddy at its boundary – the largest closed contour enclosing the eddy. The surface area is computed as the sum of the area of grid cells occupied by the eddy, which allows for non-circular eddies. The diameter of the eddy is estimated from the circle with the same area as the eddy. In other words, it is twice the equivalent length of an eddy (Chelton et al., 2007). The software can be downloaded from `https://github.com/jfaghm/OceanEddies`. A complementary Matlab toolbox to

analyse the output of the software is available at `https://doi.org/10.5281/zenodo.8025841`.

3.3 Computation of the meridional transport by coherent eddies

We computed the meridional transport of tracers by long-lived eddies across the SAF into the Subantarctic Zone using the method traditionally applied to study coherent ring structures from shipboard measurements (Joyce et al., 1981; Peterson et al., 1982; Morrow et al., 2004; Ladd et al., 2007; Patel et al., 2019, 2020). We apply this method to both observations and model to enable a direct comparison between the two. In this approach, the transport of a tracer is derived from the available tracer content anomalies and the nature of the eddy trajectories (Patel et al., 2019). The transport computation is composed of two steps.

The first step is to determine the total available tracer content for each eddy realisation (each day in the simulation). The total available content is defined as the integrated quantity of a tracer contained in the eddy after all isopycnals are flattened, allowing us to estimate the quantity of tracers that an eddy can relocate permanently due to mixing and water mass modification along isopycnals (Joyce et al., 1981). This method enables the separation of horizontal changes in water masses from changes in the vertical position of isopycnals associated with available potential energy. Consequently, it allows us to accurately determine the total trapped tracer content in the eddy core and its subsurface extent and hence the impact of the eddy on the ambient waters (Joyce et al., 1981; Peterson et al., 1982; van Ballegooyen et al., 1994).

We calculate the available tracer anomalies of each eddy referenced to its ambient surrounding waters using potential density (σ) as the vertical coordinate. The anomalies in each of the discrete σ layers are summed vertically first and then integrated over the area of the eddy, assuming axis-symmetry. Therefore, the total available heat, salt and nitrate anomaly for a given radial transect can be written as, respectively:

$$\mathcal{H} = \int_{r=0}^{R} 2\pi r \cdot \rho_i C_p h_i [T_{\sigma_i} - T_{\sigma_i}(ref)] \cdot dr \tag{1}$$

$$\mathcal{S} = \int_{r=0}^{R} 2\pi r \cdot 0.001 \rho_i h_i [S_{\sigma_i} - S_{\sigma_i}(ref)] \cdot dr \tag{2}$$

$$\mathcal{N} = \int_{r=0}^{R} 2\pi r \cdot 1000 h_i [N_{\sigma_i} - N_{\sigma_i}(ref)] \cdot dr \tag{3}$$

Here, T, S, and N are vertical profiles of conservative temperature (°C), absolute salinity (g kg^{-1}) and nitrate (μmol L^{-1}) along a radial transect through the eddy, respectively; C_p is the specific heat capacity of seawater from GSW toolbox; h_i is the thickness of the isopycnal layer in meters. The constant 0.001 in equation 2, converts grams to kilograms, and 1000 in equation 3, converts per litres to per cubic meters. The algorithm to perform this computation is provided in Patel et al. (2019, 2020).

The total available tracer anomalies are computed between potential density contours of 26.5 to 27.5 kg m^{-3}, referenced to the sea surface (Patel et al., 2019, 2020). The upper and lower density limits are determined based on T-S diagrams, to encapsulate most of the water-mass variability between the eddy core and corresponding reference profile (Fig. 5 and S4). The isopycnal range of 26.5 and 27.5 covers the depth range approximately from the sea surface to ∼1000 m at the centre and ∼1200 m at the edges of the eddy in the Subantarctic Zone. It is the same range used in Patel et al. (2019) and, therefore, allows direct comparison with their observed meridional transports by cyclonic eddies.

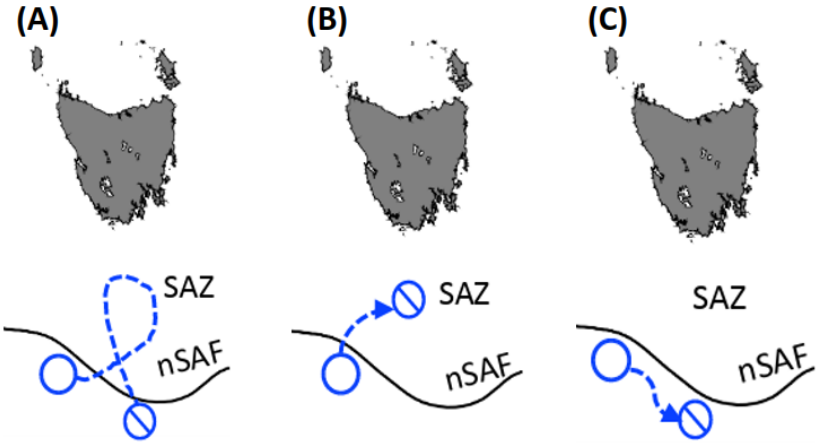

Figure 1. Illustration of the meridional transport of tracers by coherent cyclonic eddies in the Southern Ocean south of Tasmania. Open circles denote the formation of mesoscale eddies, while circles with diameter denote dissipation. SAZ stands for Subantarctic Zone, and nSAF represents the northern branch of the Subantarctic Front, depicted as a contour line. In Case A, eddies dissipate in the Subantarctic Front after traversing into the Subantarctic Zone. In Case B, eddies dissipate in the Subantarctic Zone after detachment from the front. In Case C, eddies remain in the Subantarctic Front.

The second step is to categorise the pathways of the eddies to estimate how much of the eddy content anomaly is delivered to the Subantarctic Zone as the eddy decays over its lifespan. The simulated eddies were divided into three cases based on inspection of animations, as in Patel et al. (2019, Fig. 1). Case A: a return frontal eddy detaches and then rejoins the SAF before dissipating (Fig. 1A). Its contribution to meridional transport would be its maximum tracer content minus the tracer content when it was last detected. Case B: a dissipating frontal eddy dissipates in the Subantarctic Zone after detaching from the SAF (Fig. 1B). Its contribution to meridional transport is defined to be its maximum tracer content anomaly over its lifespan. Case C: a frontal mixing eddy never leaves the SAF and does not contribute to tracer transport into the Subantarctic Zone, as it simply advects tracers along the SAF (Fig. 1C). Anticyclonic eddies did not cross the front and were always of the Case C in both model and altimetry in this region (Fig. S1, S2).

The contribution of return frontal eddies (Case A) and dissipating frontal eddies (Case B) are summed to estimate total meridional transport by coherent eddies into the Subantarctic Zone over the study period (2007-2014). The annual mean meridional transport is computed by dividing the transport by the number of study years.

3.4 Computation of the meridional transport by all transient processes

Reynolds decomposition has been used extensively to understand the transport of properties in the ocean. For example, the time-mean meridional transient heat flux ($\overline{THF}$) is traditionally computed as the covariance of velocity and temperature anomalies at each point: $\overline{THF} = \rho C_p \overline{v'T'}$ (W m^{-2}), where the overbar represents a time-mean (e.g. Jayne & Marotzke, 2002). Here, $v' = v - \overline{v}$ (m s^{-1}) and $T' = T - \overline{T}$ (°C) are the temporal anomalies of the meridional velocity and temperature with respect to the time-mean velocity ($\overline{v}$) and temperature ($\overline{T}$) computed over the study period.

Meridional THF includes both rotational and divergent components (Marshall & Shutts, 1981). The rotational component recirculates heat locally, and only the divergent component of the THF is dynamically important (Marshall & Shutts, 1981; Jayne & Marotzke, 2002). We computed this divergent THF using the Watts et al. (2016) approach. Their study demonstrated that the total geostrophic velocity (U_{Tot}) throughout a water column can be expressed as the sum of a depth-varying bottom-referenced

baroclinic velocity (U_{bcd}) and a depth-independent reference velocity (U_{ref}) that is the absolute velocity measured near the sea floor, above the bottom boundary layer (Appendix B). The U_{ref} is responsible for the divergent component of the heat fluxes, while U_{bcd} is purely non-divergent when derived from thermal wind shear on a f-plane (Watts et al., 2016; Foppert et al., 2017). Thus, the time-mean, depth-integrated, divergent, meridional THF (W m^{-1}) is calculated at each grid point of the model as:

$$\overline{THF_d} = \rho C_p \int_{-2000m}^{0} \overline{v'_{ref} T'} dz \tag{4}$$

Where subscript d is for divergent component, v'_{ref} is the near bottom velocity fluctuations, dz is the thickness of each model depth cell. The OFAM3-JRA55 uses z^* coordinates. In z^* coordinates, the thickness of every cell in the water column varies with the sea surface height. However, we used constant dz in time for the integration. Typically, this requires a small correction to the integral quantity on the order of cm or even 10s of cm relative to the water column of a few 1000 m. The algorithm to compute the transient flux is provided in Appendix B.

The transient fluxes are vertically integrated from the sea surface to 2000 m depth (model depth of 1985.3 m). OFAM3-JRA55 is restored to climatological values below 2000 m (Zhang et al., 2016). Furthermore, high-resolution modelling studies over the Southern Ocean show that transient heat and salt fluxes become negligible below 2000 m (Jayne & Marotzke, 2002; Meijers et al., 2007).

The time-mean, depth-integrated, divergent, meridional Transient Salt Flux ($\overline{TSF_d}$) and Nitrate Flux ($\overline{TNF_d}$) at each grid point are computed similarly, as:

$$\overline{TSF_d} = \int_{-2000m}^{0} \overline{v'_{ref} S'} dz \tag{5}$$

$$\overline{TNF_d} = \int_{-2000m}^{0} \overline{v'_{ref} N'} dz \tag{6}$$

Where, $S' = S - \overline{S}$ are salinity fluctuations and $N' = N - \overline{N}$ are nitrate fluctuations relative to their respective time-mean fields. We calculate salt flux, rather than freshwater flux, following Tréguier et al. (2014). Since the model uses a Boussinesq approximation (Zhang et al., 2016), salt transport is expressed in m^2 s^{-1} PSU per unit length along a latitude circle. The units for nitrate transport are mmol s^{-1} per unit length along a latitude circle.

We computed the transient fluxes from daily time-series at each grid point from the model output accounting for many events over the record, thereby ensuring a statistically stable estimate of the fluxes over the 8-year averaging period (Watts et al., 2016). We tested the sensitivity of the time-mean tracer transport to the averaging period, by calculating time-mean tracer transport for three overlapping periods of 4-years each. The area-averaged (47-55.5°S, 135-155°E) meridional transport over the three periods is within 2 to 4% of the time-mean computed over the period of 8 years (Table S3).

The Reynolds decomposition method here considers all variability between periods of 2 days and 8 years, comprising coherent eddies, waves, transient meanders and filaments as well as seasonal and interannual variability, all of which could be present in the ocean model. Our study aims to quantify the contribution of mesoscale eddies to the total transient transport, by considering all transient components. This approach allows us to isolate the contribution of mesoscale eddies, as observed using *in situ* measurements due to watermass trapping, to the overall transient transport across the Subantarctic Front in our region.

4 Model evaluation

We demonstrate that the model's representation of mesoscale processes is consistent with available observations, suggesting the suitability of the model to explore the role of eddies in the transient transport of heat, salt, and nitrate. Our evaluation involved several aspects. First, we examined the distribution of eddy kinetic energy (EKE) in OFAM3-JRA55 and compared it with altimetry. Then, we conducted an eddy census in both model and altimetry and assessed their agreement, including the evolution of kinematic characteristics over eddy lifespans and trajectories. Finally, we performed a case study to evaluate the vertical structure of a cyclonic eddy by comparing a simulated eddy to *in situ* observations of the eddy that sampled during IN2016_V02 voyage.

4.1 Eddy kinetic energy

EKE is computed from the fluctuations of the surface velocity as $EKE = 0.5(u'^2 + v'^2)$, where $u' = u - \overline{u}$ and $v' = v - \overline{v}$ are daily fluctuations in zonal and meridional velocity computed from the long-term mean, 1993-2012, to be consistent with velocity fluctuations calculated from altimetry outputs. To illustrate the spatial distribution of EKE,

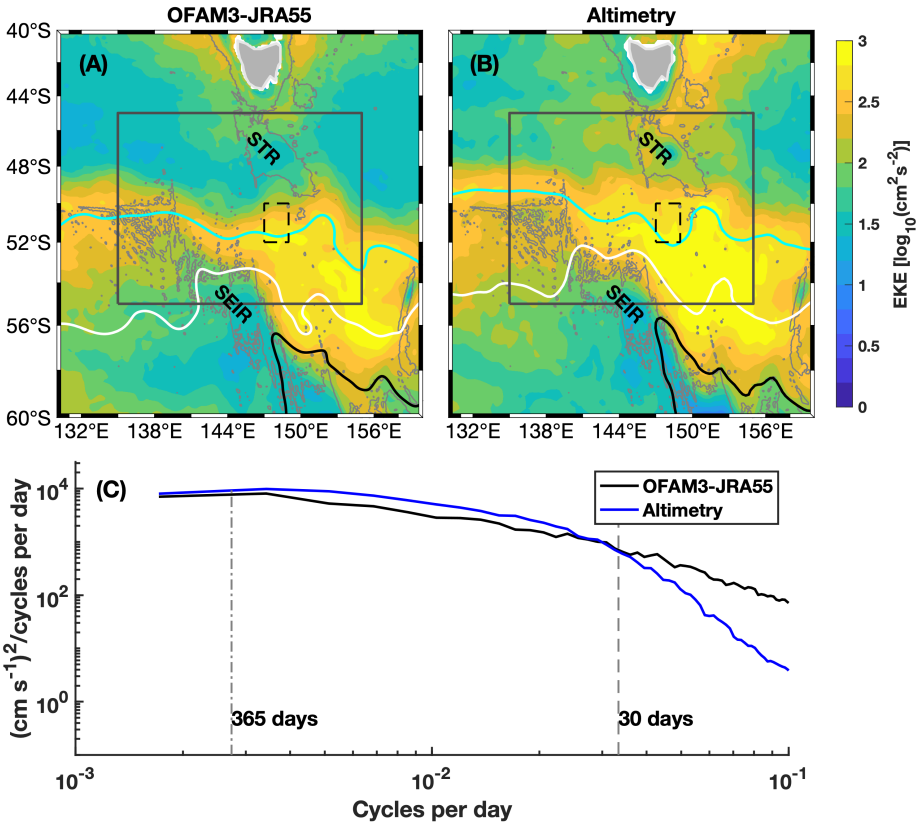

Figure 2. Spatial distribution of Eddy Kinetic Energy (EKE) from the simulation (A) and satellite observations (B) averaged over 8 years (2007-2014). The spectra of EKE (C) from the simulation and observations over 2°× 2° box (50°S – 52°S; 147°E – 149°E) denoted as a dashed box in A and B. The box is located near the eddy sampling site. The mean position of the northern and southern branches of the Subantarctic Front, and the Polar Front are represented as contours (cyan, white and black, respectively). Solid box denotes the area over which the eddy census is conducted. Grey contour of the 3000 m bathymetry highlights the Southeast Indian Ridge (SEIR) and South Tasman Rise (STR).

we averaged the EKE ($\overline{EKE}$) time-series at each grid point (Fig. 2 A and B) over the 8-year period (2007-2014).

The historical simulation realistically reproduced major energetic regions and local $\overline{EKE}$ maxima (Fig. 2 A and B). The most energetic region is found just downstream of the Southeast Indian Ridge, where the ACC fronts turn southeastward (Morrow et al., 1994; Phillips & Rintoul, 2000). This energetic region is associated with a meandering of the fronts and formation of mesoscale eddies. The simulated maximum $\overline{EKE}$ over the study region is 17% lower than the observed $\overline{EKE}$. The difference is greatest just downstream of the ridge near 148°E (Fig. 2 A and B). Although the model has weaker $\overline{EKE}$, it displayed a remarkably similar spatial structure to the observed $\overline{EKE}$. Furthermore, the local maximum $\overline{EKE}$ occurs in the location of a standing meander of both the Subantarctic Front (SAF) and Polar Front (PF) in both model and observations. The largest EKE values were contained between the northern branch of the SAF and the PF in both the model and observations (Fig. 2 A and B).

We compared the spectra of EKE from the model and observations (Fig. 2 C). The spectra were computed over a $2° \times 2°$ box in a high EKE region, encompassing the location of the eddy sampling site on the voyage (dashed box in Fig. 2 A and B). The spectra were calculated from EKE time series at each grid point for both the model and observations following Percival et al. (1993). We also analysed the spectra in several additional $2° \times 2°$ boxes in the larger eddy census domain (not shown) and found that the spectra were not sensitive to the box location.

The simulated EKE in the eddy frequency band (30 to 365 days or 0.033 to 0.0027 cycles/day) was comparable to that for the observed EKE (Fig. 2 C). We also note that OFAM3-JRA55 contained higher energy than altimetry for processes shorter than the eddy frequency (< 30 days). This difference is likely due to the higher temporal resolution of the model compared to altimetry. Although the altimeter product is daily, each altimeter track is repeated every 7 to 10 days (`https://duacs.cls.fr/`). Therefore, the time-series at any one grid point on a satellite track has inadequate information about variability with a timescale shorter than 20 days. The focus of this work is on timescales $>$ of 30 days, so the disparity between altimeter and model EKE on shorter timescales will not impact our results.

Despite some localised differences in the magnitude of $\overline{EKE}$ between the model and observations, the comparison of the EKE distribution and spectra suggested that the historical simulation represents the amount and location of energy that we find in satellite sea surface height measurements. This adds further confidence in this model simulation in addition to the model validations of Oke et al. (2013) and Zhang et al. (2016) that found Southern Ocean circulation was generally well represented in the model.

4.2 Eddy demography

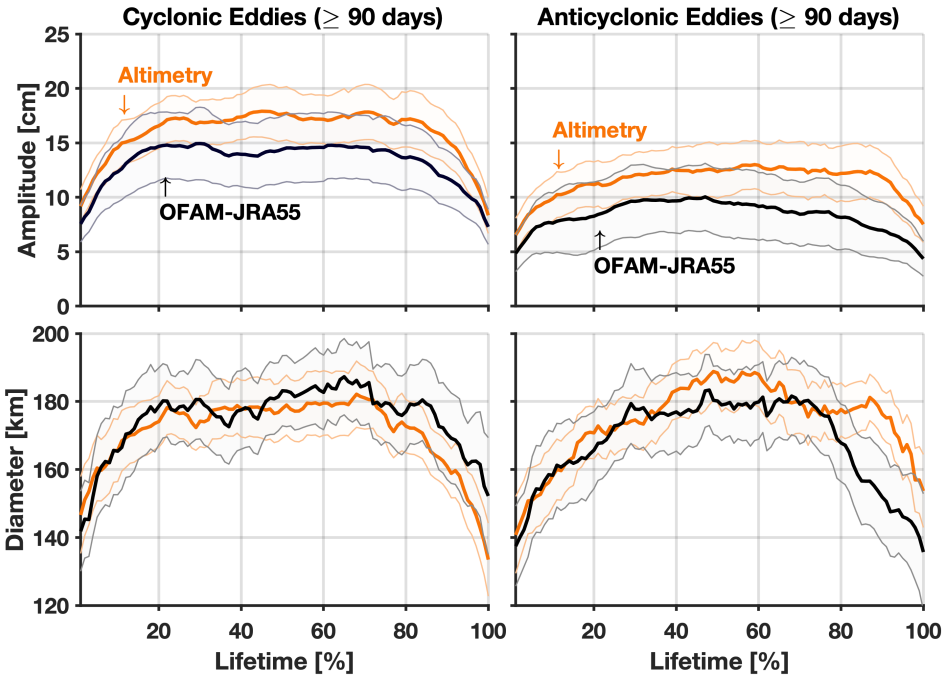

Figure 3. Composite analysis of amplitude and diameter changes over eddy lifetime. The 95% confidence bound was computed using student-t test assuming t-distribution at each life stage.

The characteristics of the eddy population were comparable between the model-based eddy census and altimetry-based census for the period 2007-2014 (Fig. A1). Focusing on long-lived eddies with a lifespan of at least 90 days, we identified a total of 14,578 eddy realisations from 99 eddies in the model and 22,500 eddy realisations from 136 eddies in the observations. The ratio of cyclones to anticyclones was similar in the model (58% cyclones) and observations (65.4% cyclones; Table A1). The surface characteristics of eddies, including rotational speed, amplitude, and diameter were positively skewed

for both cyclones and anticyclones in both model and observations (Fig. A1). This skewness indicated that the majority of eddy realisations had small values for these characteristics, while a smaller number of realisations had larger values, creating a long-tailed distribution that is consistent with previous studies (Dawson et al., 2018; Frenger et al., 2015).

Figure 3 illustrates the changes in amplitude and diameter over the lifetime of cyclones and anticyclones. In both the model and observations, cyclones had larger amplitudes than anticyclones, while the eddy diameter remained similar throughout their lifespan. Simulated eddies tended to have smaller amplitude than observed eddies (Fig. 3, top panel). However, the diameter was approximately the same between simulated and observed eddies (Fig. 3, bottom panel).

Overall, the eddy census from OFAM3-JRA55 and altimetry indicated that our study region has more cyclones than anticyclones and that cyclones have a larger amplitude and similar diameter compared to anticyclones. These results are consistent with altimetry based studies conducted over longer time periods (Frenger et al., 2015; Dawson et al., 2018, 1997-2010 and 1997-2012, respectively), indicating that the extension of the study period for the comparison will not qualitatively change the presented results. Furthermore, these results suggest that OFAM3-JRA55 performed well in capturing coherent mesoscale eddies and their surface characteristics.

4.3 Eddy propagation

We next evaluated the skill of OFAM3-JRA55 in capturing the eddy propagation direction, as it determines the contribution of eddies to the meridional transport of tracers (Morrow et al., 2004; Patel et al., 2019, 2020, Section 5.1). A composite map of eddy trajectories is constructed (Fig. 4) where each eddy trajectory is shifted such that its origin lies at the position (0,0). This technique allows us to investigate the general tendency of an eddy's propagation from its formation (Chelton et al., 2011). Eddies generally propagate westward (Chelton et al., 2007, 2011). However, due to the influence of varying zonal background flow, some eddies in the ACC propagate eastward from their formation (Frenger et al., 2015).

Eddy trajectories from the model were consistent with the observed eddy trajectories (Fig. 4). About 33% of simulated cyclones propagated eastward, with $\Delta\text{lon} > 0$.

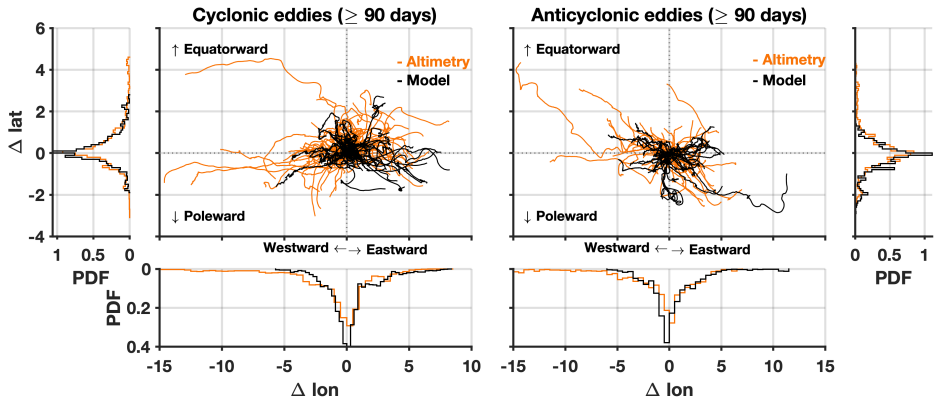

Figure 4. Composite analysis of eddy propagation directions when all the eddies start from the formation point (0, 0). The X and Y axes denote relative changes in longitudinal and latitudinal displacement, respectively. These changes in the displacements are presented as histogram in the side panels. The two large panels show all tracks, but the longer tracks obscure many eddy paths.

Approximately 22% of simulated cyclones propagated westward, with Δlon < 0. The remaining 45% travelled both eastward and westward from their origin. Similarly, in altimetry, 30% of cyclones propagated eastward, while approximately 29% propagated westward. The remaining 41% of altimeter-based cyclones travelled in both eastward and westward directions from their origin. For anticyclones, approximately 36% propagated eastward in the simulation and 34% in altimetry, 26% moved westward in the simulation and 28% in altimetry, and the remaining 38% alternated eastward and westward propagation (Fig. 4).

Regarding meridional deflection, in the simulation (altimetry), about 25% (33%) of the total cyclones moved equatorward (Δlat > 0 for an eddy track) and only 10% (15%) moved poleward (Δlat < 0) from their origin. In the case of anticyclones, only 5% (17%) moved equatorward and about 29% (21%) poleward from their origin.

We also note that simulated eddies travelled somewhat smaller distance on average than observed eddies. The mean distance travelled by the simulated cyclones was about 92% of that for observed cyclones. The mean distance travelled by the simulated anticyclones was about 89% of that for observed anticyclones. Overall, OFAM3-JRA55 represents eddy trajectories and their propagation distance well; however, some observed

eddies travelled much further from their origin than the simulated eddies (westward or north-westward), potentially due to the longer lifespan of observed eddies.

4.4 Vertical structure of mesoscale eddies in OFAM3-JRA55

We compare the subsurface structure of cyclonic eddies in the model with a detailed shipboard survey of an actual cyclonic eddy that originated in the SAF (Patel et al., 2019, 2020). To this end, we selected one simulated cyclonic eddy to compare the subsurface vertical structure of mesoscale cyclonic eddies in the model with observations. We chose not to use a composite eddy for the comparison because the subsurface vertical distribution of physical and biogeochemical properties in the model eddies varies with age. Furthermore, the composite eddy structure studies based on altimetry and Argo observations show strong geographical dependence of the evolution of the subsurface structure of long-lived eddies due to the impact of regional circulation on the eddies' vertical structure (e.g. Pegliasco et al., 2015; Frenger et al., 2015).

The selected simulated eddy was generated in the same season and had similar surface characteristics as the observed cyclonic eddy (Table S4). Both eddies were formed in summer (Jan/Feb) and dissipated in autumn (May). After their formation in the SAF, they detached from the front and traversed into the Subantarctic Zone before returning southward and reabsorbing into the front (Fig. S3). The median rotational speed, amplitude, and diameter of the simulated cyclonic eddy were lower than the observed cyclonic eddy by 49%, 40%, and 14%, respectively (Table S4), as expected from the overall eddy statistics (Section 4.2). The lifespan of the simulated and the observed cyclonic eddies was similar; however, the observed eddy travelled about 23% further.

Figure 5 illustrates the comparison of vertical transects of temperature, salinity, and nitrate between the simulated and observed eddies, revealing a remarkable similarity between the two. However, the simulated eddy exhibited less intense doming of isopycnals than the observed eddy. For example, the 27.2 kg/m^3 isopycnal was elevated from about 600 dbar at the edge of the eddy to 450 dbar in the centre, exhibiting an uplift of 150 dbar in the simulated eddy, whereas the same isopycnal uplifted by 275 dbar in the observations.

Both eddies carried anomalously cold, fresh, dense, and nitrate-rich water in their core compared to surrounding water (Fig. S4 and S5). However, the maximum temper-

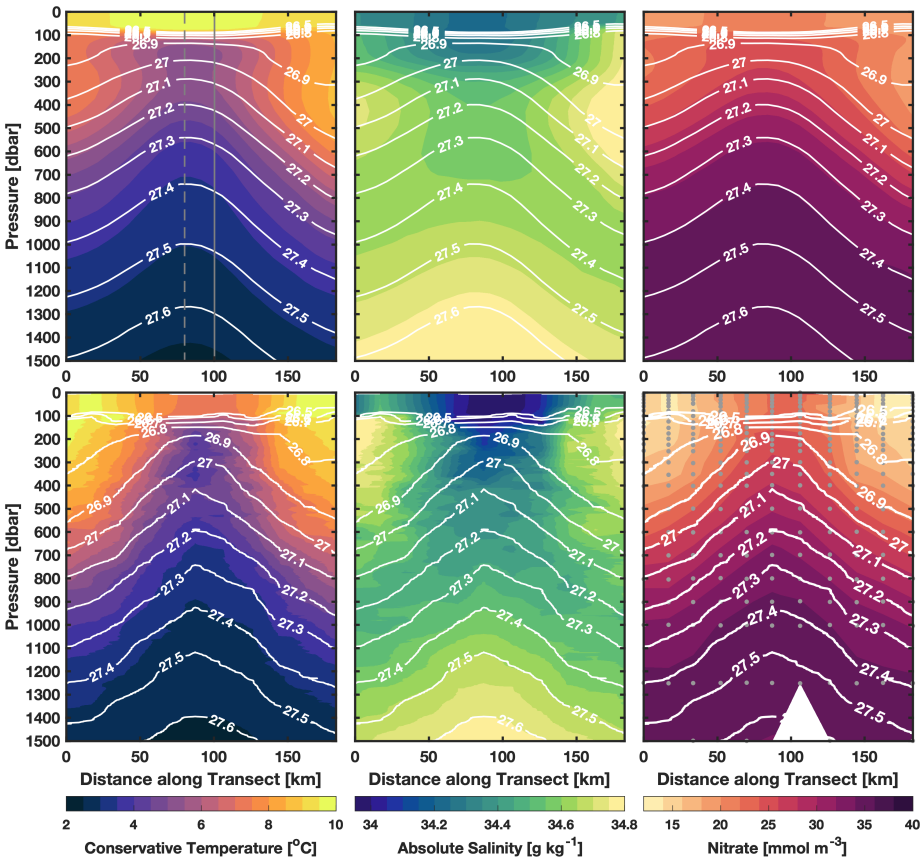

Figure 5. Vertical distribution of conservative temperature, absolute salinity and nitrate across the simulated eddy (top panels) and the observed eddy (bottom panels) in the declining phase of an eddy as shown in Fig S3. The potential density contours are superimposed for both eddies. The vertical dashed line denotes the centre of the isopycnal doming. The vertical solid line denotes the eddy centre detected from the simulated sea surface height.

ature, salinity, and nitrate anomalies in the simulated eddy were about 65%, 50%, and 70% of the observed anomalies, respectively. We also note a warm anomaly in the top 100 m of the simulated eddy. This could be because the atmospheric boundary layer properties are prescribed by JRA-55 forcing, leading to damping of the temperature anomalies in the surface layer compared to the actual damping of the coupled system.

In OFAM3-JRA55, the eddy centre detected from the sea surface height and the isopycnal elevation centre were slightly offset (Fig. 5, top panel, vertical lines). This behaviour was more prominent as the eddy aged. Nevertheless, the evaluation of the model skill against a single snapshot of observations, both at the beginning of the declining phase of the eddy, indicated that OFAM3-JRA55 captured the subsurface structure of cyclonic eddies reasonably well (Fig. 5).

5 Meridional transport from OFAM3-JRA55

With the confidence in the model skill, we next estimate the relative importance of mesoscale eddies in the meridional transport of tracers by all transient processes. To this end, we compare the meridional transport by all transient processes (Section 3.4) to that by coherent eddies directly (Section 3.3) from the same model output.

5.1 Transport by individual coherent eddies

We calculated the meridional transport of heat, salt, and nitrate for each simulated eddy realisation over its lifetime in the Subantarctic Zone, applying equation 1-3 to the 3-dimensional model output (Section 3.3). In our study region, a total of 26 simulated cyclones were formed through the instability of the northern and southern branches of the SAF during the study period. Of these simulated cyclones, only 11 contributed to meridional transport (Section 3.3): 3 are categorised as dissipating frontal eddies, 8 as return frontal eddies, and the remaining 15 cyclones are frontal mixing eddies that do not transport tracers into the Subantarctic Zone.

The total meridional transports by these long-lived cyclones into the Subantarctic Zone over the course of 8 years are tabulated (Table 1). On average, a dissipating frontal eddy transfers -0.9×10^{20} J of heat, -4.4×10^{12} kg of salt and 3.9×10^{10} mol of nitrate. Likewise, a return frontal eddy transfers -0.72×10^{20} J of heat, -3.2×10^{12} kg of salt, and 2.78×10^{10} mol of nitrate.

Combining both types of eddies, we found annual tracer transports of $-1.06\pm0.3\times10^{20}$ J year^{-1} (cooling) for heat, $-4.85\pm1.3\times10^{12}$ kg year^{-1} (freshening) for salt and $4.23\pm1.4\times10^{10}$ mol year^{-1} (fertilising) for nitrate into the Subantarctic Zone over the 20° longitude band (135°E to 155°E). The variability in the annual transport is computed as the standard deviation of mean transports when the transports associated with dissipating frontal eddies and return frontal eddies are combined.

Table 1. Total tracer transport by the long-lived cyclones across the Subantarctic Front into the Subantarctic Zone over the period of 8 years (2007-2014) in the longitude range 135°E to 155°E, integrated over the density range (σ_θ = 26.5 to 27.5). The variability in the transport is computed as standard deviation. Standard deviation computed for each type of eddy pathway over the respective number of eddies, and then summed for the total variability.

Eddy Pathway	No. of Eddies	Heat ($\times10^{20}$J)	Salt ($\times10^{12}$kg)	Nitrate ($\times10^{10}$mol)
Dissipating Frontal eddy	3	-2.70 ± 0.35	-13.2 ± 1.8	11.6 ± 0.7
Return Frontal eddy	8	-5.75 ± 0.18	-25.6 ± 0.8	22.3 ± 1.1
Frontal Mixing eddy	15	0	0	0
Total transport	26	-8.45 ± 0.53	-38.8 ± 2.6	33.9 ± 1.8
Annual transport		-1.06 ± 0.3	-4.85 ± 1.3	4.23 ± 1.4

The formation of anticyclones through SAF instability was primarily limited to frontal mixing eddies. Out of 42 simulated anticyclones, only 18 originated in the SAF and 16 propagated along the meander rather than moving directly (northward or southward) across the front. These patterns are consistent with observed cyclones and anticyclones (Fig. S1 and S2), as well as the previous findings of Morrow et al. (2004) and Pilo et al. (2018). Both studies showed that most anticyclones in the Southern Ocean south of Tasmania are formed either due to instability of the East Australian Current or the interaction between the SAF and the South Tasman Rise. Therefore, anticyclones did not contribute to meridional transport of their content out of the Subantarctic Zone over this time period.

5.2 Transport by transient processes

The spatial distribution of the mean temperature, salinity, and nitrate, computed over the study period, are shown in Figure 6 (top panel). The time-mean, divergent, meridional flux of heat, salt, and nitrate by all transient processes from Equations 4-6 applied to the model output is shown in Figure 6 (bottom panel).

The spatial distribution of vertically integrated transient fluxes exhibit spatial heterogeneity, with the strongest transports observed in a standing meander, in the flow downstream of the Southeast Indian Ridge (Fig. 6, bottom panel). Along the northern branch of the Subantarctic Front (SAF), there are pronounced southward heat fluxes ($>$ 100 MW/m) that extend southward to the Polar Front (PF) downstream of the Southeast Indian Ridge (Fig. 6, D). Smaller equatorward heat fluxes ($\sim$70 MW/m) are observed in localised patches across the northern branch of the SAF (approximately between 50.7°S and 52.7°S, and 148°E to 149°E), as well as between the southern branch of the SAF and the PF (55°S and 150°E). This positive time-mean, divergent, depth-integrated, meridional heat flux ($\overline{THF_d}$) could be due to a residual rotational component in the transient heat flux (Watts et al., 2016; Foppert et al., 2017). Overall, the majority of the $\overline{THF_d}$ vectors in the region are southward, indicating that net transient heat transport is directed poleward and down the mean temperature gradient, as expected.

The spatial distribution of time-mean, depth-integrated, divergent, meridional transient salt flux ($\overline{TSF_d}$) exhibits similarities to that of heat (Fig. 6, D and E). Strong poleward salt fluxes (> -0.5 m^2/s PSU) are primarily confined between the northern and southern branches of the SAF, while weaker but still poleward fluxes (< -0.5 m^2/s PSU) are present between the southern branch of the SAF and the PF. Similar to the heat flux, we also observed localised patches of equatorward $\overline{TSF_d}$ across the northern branch of the SAF, as well as some equatorward $\overline{TSF_d}$ (> 0.5 m^2/s PSU) between the southern branch of the SAF and the PF (Fig. 6, E), where heat transport was poleward (Fig. 6, D).

These findings of strong poleward fluxes of heat and salt across the SAF and their heightened magnitudes downstream of an oceanic ridge corroborate previous global model studies conducted by Meijers et al. (2007) and Tréguier et al. (2014). These prior studies have substantiated that, in a zonal average, the strongest poleward fluxes align with the SAF. Furthermore, transient heat fluxes exhibit a peak downstream of oceanic ridges,

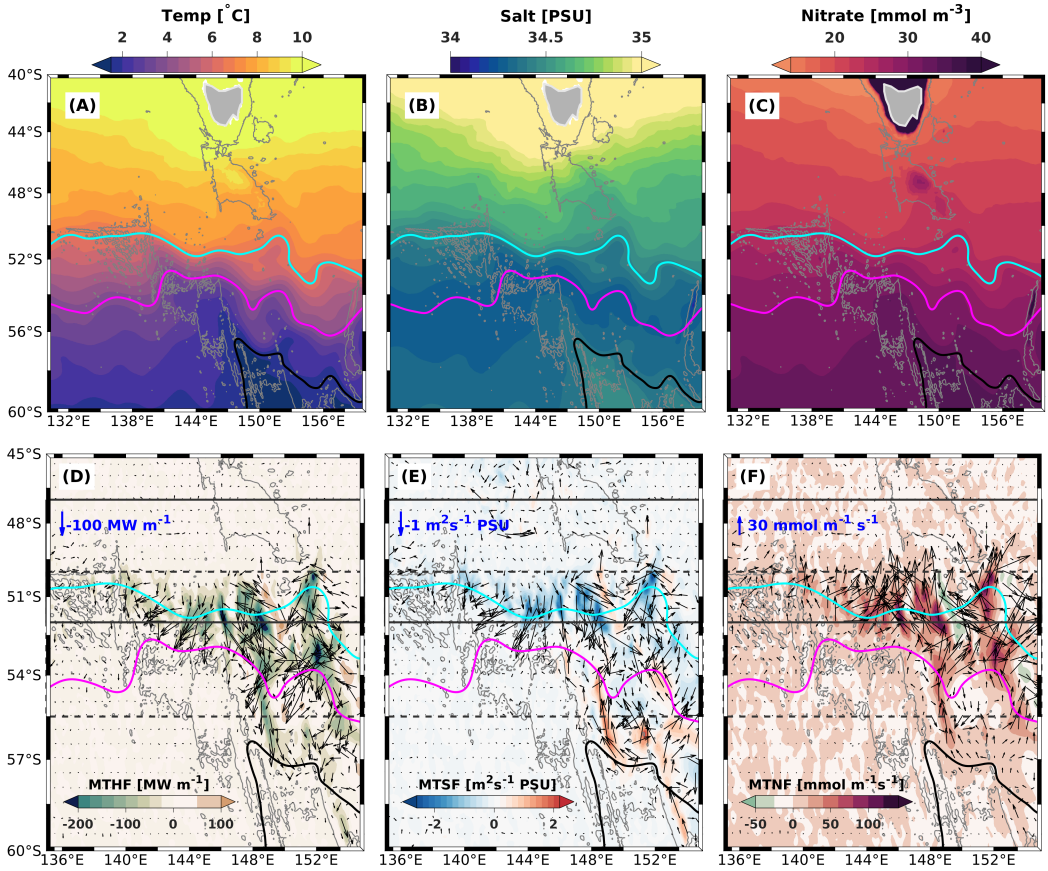

Figure 6. Climatological distribution of temperature (A), salt (B) and nitrate (C) from OFAM3-JRA55 averaged over the study period and spatial distribution of time-mean depth-integrated, divergent, meridional transient heat flux (D), salt flux (E) and nitrate flux (F). Vectors of transient fluxes are superimposed by computing the time-mean depth-integrated, divergent zonal transient fluxes (D, E, F). Grey contour represents 3000 m bathymetry. The mean position of the northern (cyan) and southern (magenta) branches of the Subantarctic Front and the Polar Front (black) are shown as contours. The solid and dashed boxes delimit the Subantarctic Zone, Subantarctic Front Zone, respectively in the bottom panel.

creating a prominent hotspot for cross-frontal transport facilitated by increased topographic steering (Thompson & Naveira Garabato, 2014).

The time-mean, depth-integrated, divergent, meridional transient nitrate flux ($\overline{TNF_d}$) exhibited a localised patchiness and predominantly equatorward pattern, which is down the mean nitrate gradient across the ACC (Fig. 6, C and F). The areas of strong equatorward nitrate transport coincided with regions of intense poleward heat and salt fluxes. No previous study has specifically documented the pattern of enhanced nitrate fluxes in the presences of meanders. The location of the equatorward nitrate transport may be a unique feature of this region and warrants further investigation to understand its underlying mechanisms and implications.

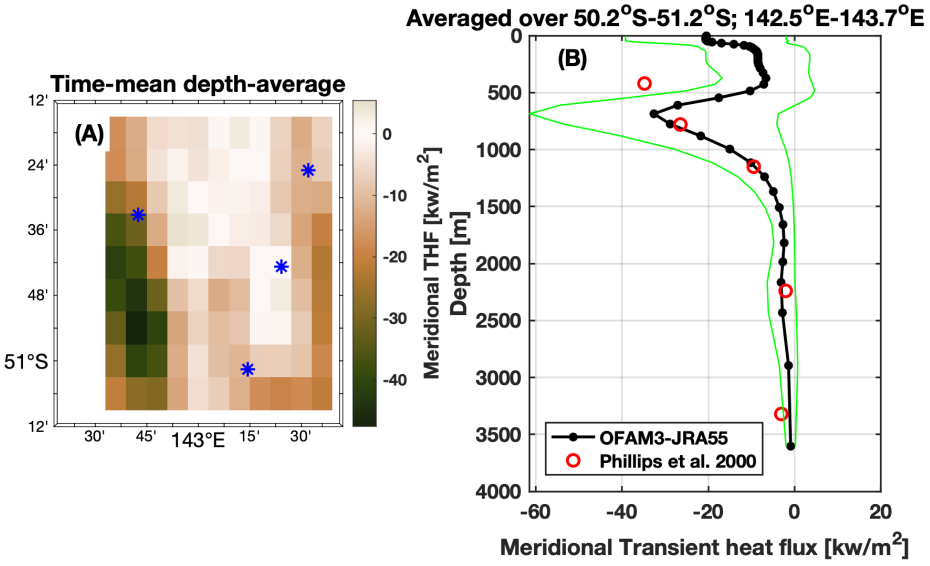

Figure 7. Time-mean, depth-averaged, divergent, meridional transient heat flux from OFAM3-JRA55 for 2007-2014. Blue asterisks denote positions of the four mooring positions (Phillips & Rintoul, 2000, A). Area-averaged model time-mean, divergent, meridional transient heat flux (black line, B) with one standard deviation envelope (green lines). Red dots are the mean observed meridional transient heat fluxes from the four moorings in panel A.

We compared our transient heat flux estimate from the model with the best estimate of the observed transient heat flux, obtained from mooring time-series near 143°E, 51°S (Phillips & Rintoul, 2000, Fig. 7). The comparison revealed good agreement between the model and observations below a depth of 500 m (Fig. 7, B). Above 500 m, the

591 model based THF was lower by a factor of approximately 5. The observed profile rep-
592 resents an average over a two-year period (1993-1995), and across four moorings, whereas
593 the model profile represents a temporal average over 8 years (2007-2014) and a spatial
594 average over the region of the moorings (Fig. 7, A). Thus, spatial and temporal differ-
595 ences could account for the disparity in the estimates (Figure 7, B). It is remarkable that
596 the model average profile overlies the observed estimates within the range of variabil-
597 ity ($\pm 1\sigma$), below 500 m. The weaker upper ocean THF_d in the model may also be at-
598 tributed to the weaker eddy variability simulated in the OFAM3-JRA55 (Fig. 2). A sim-
599 ilar comparison for salt and nitrate was not possible due to a lack of observations.

600 In summary, intense poleward fluxes occur at the location of strong meanders in
601 the flow downstream of the Southeast Indian Ridge. The equatorward transport of ni-
602 trate across the SAF and PF is colocated with strong poleward transport of heat and
603 salt. The transport across the SAF is much more widespread and intense than the trans-
604 port across the PF, as also shown by Foppert et al. (2017) for the heat fluxes.

605 ### 5.3 Importance of coherent eddies in the tracer transport

606 There is a disconnect between estimates of poleward "eddy" transport constructed
607 from (1) shipboard surveys of coherent eddies combined with eddy tracking from altime-
608 try (Morrow et al., 2004; Swart et al., 2008; Patel et al., 2019); and (2) estimates based
609 on Reynolds decomposition of time series in observations (Phillips & Rintoul, 2000; Watts
610 et al., 2016) and models (Jayne & Marotzke, 2002; Meijers et al., 2007; Tréguier et al.,
611 2014). The first provides the eddy tracer transport from coherent eddies and the second
612 provides transport from all transient processes, including coherent eddies. Here, we rec-
613 oncile these two approaches through the application of both to the historical simulation
614 of OFAM3-JRA55, which was confirmed to simulate eddies realistically.

Table 2. Meridional transport by long-lived coherent eddies and all transient processes in OFAM3-JRA55. The estimate for transient processes is obtained by averaging over south of Tasmania, 47°S-55.5°S and 135°E-155°E to be consistent with Patel et al. (2019).

Transport	Heat (MW m^{-1})	Salt ($\mathrm{m}^2\ \mathrm{s}^{-1}$ PSU)	Nitrate (mmol $\mathrm{m}^{-1}\mathrm{s}^{-1}$)
coherent eddies	-2.4 ± 0.09	-0.11 ± 0.004	0.96 ± 0.023
transient processes	-14.5 ± 1.6	-0.098 ± 0.014	6.61 ± 0.74

The total poleward transport of heat by all transient processes ($\overline{THF_d}$), including coherent eddies, in OFAM3-JRA55, averaged over the study region, was -14.5 MW m^{-1} (Table 2). In Section 5.1, we found that long-lived simulated cyclones transported -1.06×10^{20} J $year^{-1}$ of heat poleward across the Subantarctic Front (SAF) in the longitude band 135°E-155°E. This transport can be expressed in terms of the depth-integrated meridional heat flux per meter of the basin length (1.4×10^{6} m), which is -2.4 MW m^{-1}. Consequently, coherent long-lived cyclones carried approximately 17% of the total poleward heat transport across the SAF south of Tasmania. This proportion is roughly the same as estimated by Patel et al. (2019, 21%), who combined *in situ* and altimetry observations to quantify mean poleward heat transport by long-lived eddies and their contribution to the total eddy transport using Foppert et al. (2017)'s sea surface height-based proxy. The close agreement between our estimate and Patel et al. (2019) suggests that surface proxies are reliable for quantifying the role of long-lived eddies in the Southern Ocean heat budget. We test this hypothesis in Section 6.

The average salt transport by all transient processes ($\overline{TSF_d}$) in OFAM3-JRA55 over the study region was -0.098 m^2 s^{-1} PSU. The salt transport across the SAF by long-lived cyclonic eddies in the 20°longitude band was -4.85×10^{12} kg $year^{-1}$ in OFAM3-JRA55 (Section 5.1). This is equivalent to a poleward flux of -0.11 m^2 s^{-1} PSU, in units of tracer transport per unit length of the basin. To achieve this, we divided the eddy transport in kg $year^{-1}$ by density (1035 kg m^{-3}) to convert from mass to volume and then by 0.001 to convert from g kg^{-1} to PSU, and finally by the zonal length (1.4×10^{6} m). Consequently, the poleward salt transport by long-lived cyclonic eddies in our study region in this model is approximately equal to the total poleward salt transport by all transient processes. It appears unlikely that all the meridional salt transport is accomplished solely by coherent eddies. This could be attributed in part to the presence of equatorward salt fluxes caused by transient processes south of the Polar Front in the model (Fig. 6, E), which reduce the area-averaged flux and may not reflect realistic behaviour.

The average nitrate transport by all transient processes ($\overline{TNF_d}$) in the model over the study region was 6.61 mmol m^{-1} s^{-1}. The nitrate transport across the SAF by long-lived cyclonic eddies in OFAM3-JRA55 was 4.23×10^{10} mol $year^{-1}$ (Section 5.1). This is equivalent to equatorward transport of 0.96 mmol m^{-1} s^{-1}, calculated by dividing the transport by the zonal length and the number of seconds in a year. Hence, the equatorward nitrate transport by long-lived cyclonic eddies in our study region in this model

constitutes around 15% of the total equatorward nitrate transport attributable to all transient processes. This nitrate transport determines the nitrate content of mode waters, consequently influencing productivity in the lower latitudes (Palter et al., 2010; Patel et al., 2020).

In the preceding results, we estimate the contribution of transient process over the entire study region. However, the transport facilitated by long-lived cyclonic eddies is predominately confined to the Subantarctic Zone (Fig. S6). The average transient tracer transport over the Subantarctic Zone south of Tasmania (47°S-52°S and 135°E-155°E) is presented in Table C1. A comparison of this regional transient transport with the concurrent transport of eddies reveals that these eddies contribute approximately 21%, 73%, and 16% to the total transient heat, salt and nitrate transport, respectively. This result indicates that the contribution of long-lived cyclonic eddies, generated due to the Subantarctic Front instability, to the regional average remains consistent with the above results. Importantly, this insensitivity to region can be attributed to the localised total transient tracer transport (Section 5.2).

Our results are consistent with those of Abernathey and Haller (2018), who demonstrated that the contribution of coherent eddies to full turbulent fluxes is small in the Pacific Ocean. Their result challenged previous studies that described estimates of coherent eddy transport based on Eulerian eddy identification methods such as those used in our study. However, the way we compute the tracer content of eddies accounts for the coherency of the eddy. Our estimate of coherent eddy heat, salt and nitrate transport is a contribution from nonlinear eddies, or Eulerian eddies, in the terminology of Abernathey and Haller (2018). Overall, our results indicate that coherent long-lived eddies introduce marginal tracer content due to trapping, in OFAM3-JRA55, underscoring the importance of short-lived eddies and other transient processes such as meanders, stirring and filamentation at the periphery of coherent eddies (Abernathey & Haller, 2018; Meijer et al., 2022). Furthermore, the eddy trapping was also found to account for a small fraction of biomass anomalies in the Southern Ocean (Frenger et al., 2018; Rohr et al., 2020).

We have not considered short-lived cyclonic and anticyclonic eddies or the contribution of long-lived eddies due to stirring effects. The transport due to all transient processes may also be underestimated, since submesoscale filaments and other small-scale processes are not resolved with this model. Another approach to quantify these processes

would be to decompose the covariance of velocity and tracer (temperature, salinity, and nutrient) fluctuations in the frequency domain, as done in mooring studies (Nowlin Jr et al., 1985; Phillips & Rintoul, 2000; Watts et al., 2016). An inherent difficulty would be to separate the divergent and rotational component of transient fluxes, as noted in Jayne and Marotzke (2002). The statistical estimate presented in this study can be substantiated by creating an ensemble of independently initialised simulations, with the same forcing but different initial conditions. This is beyond the scope of this work.

Importantly, the integration of discrete eddy estimates and Reynolds decomposition-based methods enables us to quantify the relative importance of mesoscale coherent eddies in the meridional transport of tracers attributed to all transient processes. This integrated approach enhances our ability to better constrain the poleward tracer transport budget. Furthermore, this refined understanding guides decisions regarding the parameterization of eddy effects in climate models. The current parameterization used in coarse resolution climate models accounts for the impact of eddy stirring but overlooks the trapping mechanism. Although the contribution of trapping mechanism may seem small for large-scale transport, it has substantial implications for local productivity and ecosystems. However, determining the dominant region of different mechanisms influencing transport by mesoscale eddies remains an open question.

6 ISE-proxy to monitor the transport by coherent eddies

Monitoring meridional eddy transports, even for heat, remains elusive. To address this, efforts are underway to develop proxies for meridional transport based on satellite observations and scarce *in situ* observations. For instance, sea surface height standard deviation has been proposed as a proxy for meridional transient heat transport (Foppert et al., 2017), while integrated surface elevation (ISE) has been used to estimate the subsurface tracer content of long-lived coherent eddies (Swart et al., 2008; Patel et al., 2019, 2020). By applying the ISE-proxy to altimetry-tracked eddies, it becomes possible to determine the combined transport of heat and salt (Swart et al., 2008; Patel et al., 2019) and nutrients (Patel et al., 2020) by the eddy population. However, meridional transports delivered by eddies of smaller spatial and temporal scales cannot be observed by present-day altimetry. Therefore, it is essential to quantify the contribution of eddies, that are large enough to be remotely monitored through proxy methods, to the overall meridional transport by all transient processes.

The model allows us to test the reliability of the ISE-proxy for monitoring of meridional fluxes by long-lived cyclonic eddies. Observation-based studies have shown a linear relationship between ISE derived from satellite altimeter observations and subsurface tracer content derived from hydrographic observations. This empirical relationship exists because the strongly sloping isopycnals in the Southern Ocean are dynamically linked to the water mass structure below the sea surface (Watts et al., 2001). This permits the estimation of the tracer content in all eddies in the satellite altimeter record (Swart et al., 2008; Patel et al., 2019, 2020). Typically, the empirical relationship is based on a single eddy realisation and a single hydrographic survey. Here, we use the model to determine the empirical relationship between ISE and total available tracer content, using many simulated cyclones in our region. This approach enables us to investigate the variability in the empirical relationship due to different model eddies and compare it with the relationship derived by Patel et al. (2019, 2020) using *in situ* measurements for the Southern Ocean south of Tasmania. Moreover, the identical approach is applicable to anticyclonic eddies, however its exploration is deferred for future studies.

We used 1534 eddy realisations from 11 unique cyclones to determine the empirical relationship between their ISE and subsurface tracer content anomaly. These 11 cyclones were chosen because they contributed to the transport in the SAZ (Table 1). The ISE is defined as the volume of a cone (1/3 x height x surface area), where the cone's height is the amplitude of an eddy realisation. The surface area of the eddy can be of any shape (i.e. circular or elliptical; Patel et al., 2019). The total available heat ($\mathcal{H}$), salt ($\mathcal{S}$), and nitrate ($\mathcal{N}$) anomalies were computed for each eddy realisation (Section 3.3).

We found that the total available tracer content exhibited a skewed distribution, with skewness values of -1.13 for heat and salt, and 1.67 for nitrate, suggesting many eddy realisations are likely to have negative, and positive extreme values of tracer content respectively. The median tracer content carried by an eddy realisation was estimated to be $-0.32 \pm 0.25 \times 10^{20}$ J for heat, $-1.37 \pm 1.13 \times 10^{12}$ kg for salt, and $0.78 \pm 1.1 \times 10^{10}$ mol for nitrate. These values represent the central tendency of the tracer content probability distribution within eddy realisations. To quantify the spread or variability of the distribution, we used an interquartile range. These tracer content values are consistent with regional estimates based on *in situ* observations; -0.5×10^{20} J, -2.1×10^{12} kg and 0.87×10^{10} mol for heat, salt, and nitrate, respectively (Patel et al., 2019, 2020).

Our study, therefore, captures the variability and magnitudes of tracer content in eddy realisations.

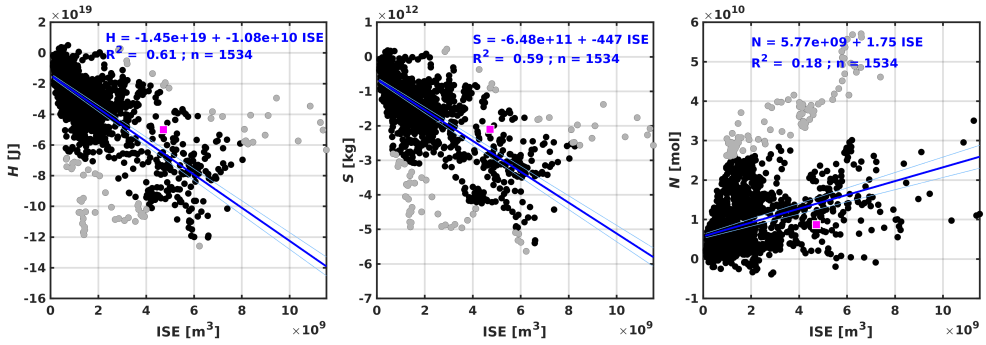

Figure 8. Relationship between total available heat, salt and nitrate content anomaly, and integrated surface elevation (ISE) of eddies. Each black dot is a realisation from 11 qualifying cyclones used to fit the relationship. The blue line represents robust regression fit and cyan lines denote upper and lower bound of the regression coefficients computed at 5% significance level. The grey dots denote realisations greater than 3 times of the scaled mean absolute deviation from the median of the residual distribution. R^2 is the coefficient of determination and n is the number of eddy realisations. Magenta square denotes total available heat, salt and nitrate content anomaly and corresponding ISE of the observed cyclonic eddy, respectively (Patel et al., 2019, 2020).

We found a statistically significant relationship between ISE and each of $\mathcal{H}$, $\mathcal{S}$, and $\mathcal{N}$ when linearly regressed, as illustrated in Figure 8. Robust regression with a bi-square weighting function was applied to reduce the influence of outliers. This robust regression fit is performed using Matlab's Statistics and Machine Learning Toolbox, employing iteratively re-weighted the least squares to compute the coefficients. The coefficient of determination (R^2) values were 0.6 for $\mathcal{H}$ and $\mathcal{S}$, and 0.2 for $\mathcal{N}$. These R^2 values indicate that approximately 60% of the variance in $\mathcal{H}$ and $\mathcal{S}$ can be explained by the variations in ISE, while approximately 20% of the variance in $\mathcal{N}$ can be explained by the variations in ISE. All three relationships were found to be statistically significant at the 95% confidence level, with p-values less than 0.05, providing strong evidence that the observed associations are not due to chance (Fig. 8). These results indicate ISE's potential to be used as a proxy.

The relatively low R^2 value for the relationship between ISE and $\mathcal{N}$ suggests that a simple linear relationship does not fully capture the complex physical and biological interactions influencing nitrate in eddies. Additional factors, such as latitude, and seasonal variations in nitrogen cycling, could potentially improve the accuracy of estimating nitrate content from ISE (Fig. S7). This warrants further investigation.

We also observed significant deviation from the relationship between ISE and both heat and salt anomalies in certain areas. For instance, the relationship appears to be less applicable for high ISE values ($> 8 \times 10^9$ m^3, Fig. 8, grey dots). These high ISE values primarily result from anomalously large surface area in some eddy realisations, as opposed to large amplitudes.

Nonetheless, the robust fit lines almost pass through the observed $\mathcal{H}$, $\mathcal{S}$, and $\mathcal{N}$ values of Patel et al. (2019, 2020) (Fig. 8, magenta squares), corroborating the connection between the surface imprint of an eddy and its subsurface contents. These results reinforce the confidence in the model's ability to represent the distribution of tracer content within cyclones that are generated due to SAF instability, consistent with previous observations in this region (Patel et al., 2019, 2020).

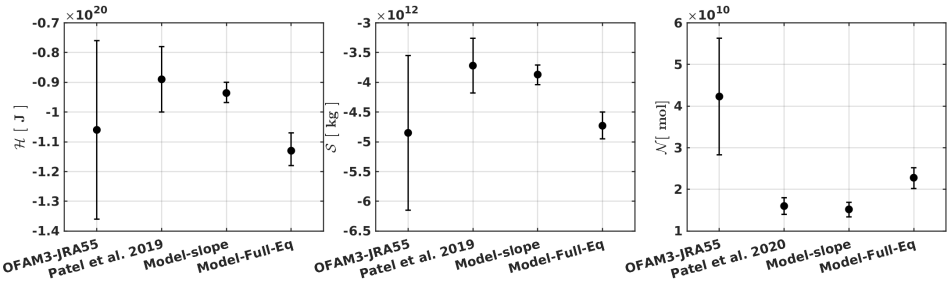

Figure 9. Comparison of the simulated meridional transport of heat, salt, and nitrate by long-lived cyclones (OFAM3-JRA55) to the meridional transport estimates from satellite observations using ISE-proxy relation based on *in situ* observations (obtained from Patel et al., 2019, 2020) and OFAM3-JRA55 (Model-slope). Model-slope represents the satellite based estimate using only the slope of the empirical relationship derived from model eddies (Fig. 8). Model-Full-Eq represents the satellite based estimate when both the slope and the intercept of the empirical relationship is used (Fig. 8). The confidence interval of the linear relationship is used to compute the variability around the mean transport for Model-proxy (Model-slope) and Model-full-Eq.

6.1 Application of ISE-proxy to satellite altimetry and assessment of tracer transport from OFAM3-JRA55

We used the ISE-proxy derived from the model and applied it to the 22-year (1993-2014) satellite record of cyclones, to compute the meridional tracer transport in our study region (135°E to 155°E, Fig. 9, Model-slope). The resulting satellite-based tracer transports fell in the bounds of the estimates made by Patel et al. (2019, 2020) for heat, salt, and nitrate transport (Fig. 9, Patel et al.). Both Patel et al. (2019) and (2020) derived their empirical relationship from a single eddy realisation and applied to the same satellite record of cyclones. The consistency between the two estimates further underpins the use of ISE as a suitable proxy for estimating the heat, salt, and nitrate content of long-lived cyclones, even when many cyclones are considered, making it a valuable tool for studying the tracer content of Southern Ocean eddies.

We compared our model's explicitly calculated tracer transports (Fig. 9, OFAM3-JRA55) with the satellite-based estimates using the ISE-proxy derived from the model and previous studies. Our simulated mean meridional heat transport was found to be -1.06×10^{20} J year^{-1}, salt transport was -4.85×10^{12} kg year^{-1} and nitrate transport was 4.23×10^{10} mol year^{-1} by eddies (Section 5.1).

When considering only the slope of the relationship, our simulated mean heat and salt transports were slightly larger than the Model-slope estimates by approximately 12% and 25%, respectively. They were also larger than the estimates from Patel et al. (2019) by around 19% and 30%, respectively. However, all the estimates of heat and salt transports were not significantly different, even when accounting for the intercept of the relationship and different numbers of eddies used in the computation of the direct estimate and ISE-proxy based estimates (Fig. 9, Model-Full-Eq).

In contrast, the directly calculated mean nitrate transport was approximately 2.5 times higher than all ISE-proxy estimates. The relationship between ISE and $\mathcal{N}$ is clearly less robust than $\mathcal{H}$ and $\mathcal{S}$. The lower significance of the ISE vs $\mathcal{N}$ regression (Fig. 8) likely contributes to the underestimate of nitrate transport when the ISE-proxy method is used (Fig. 9). This warrants further investigation to improve the proxy, either by reexamining the relationship with more observations from BGC-Argo and the GO-SHIP program or by integrating a biogeochemical model component with explicit nitrogen cycling. In addition, concerns remain about the applicability of these proxies beyond the regions with

in situ observations. Moreover, we have not separated the influence of an eddy's life-stages in the presented empirical relationship, considering the variability in tracer content. The influence of eddies that are formed due to other mechanisms in this region is also not considered.

7 Summary and Conclusions

We have brought together two research avenues, which independently seek to understand the role of eddies in the total poleward transport of tracers. To accomplish this, we applied a ship-based observational approach and a Reynolds decomposition approach to a 1/10°ocean general circulation model (OFAM3-JRA55). We have focused on the Southern Ocean south of Tasmania, a hotspot for poleward transport (Thompson & Sallée, 2012; Dufour et al., 2015; Foppert et al., 2017). We demonstrated that:

1. the OFAM3-JRA55 model has good skill in representing mesoscale variability. The surface properties of model eddies compared well with those from satellite altimetry in terms of eddy kinetic energy, eddy population demographics and propagation pathways, and the subsurface representation of temperature, salinity, and nitrate (Section 4). This evaluation revealed that the region is enriched with cyclonic eddies that have a larger amplitude, but similar diameter compared to less common anticyclonic eddies.
2. the spatial distribution of depth-integrated total transient transport of heat, salt, and nitrate based on Reynolds decomposition of the model fields is dominated by poleward heat and salt transport and equatorward nitrate transport across the northern and southern branches of the Subantarctic Front and between the Subantarctic and Polar fronts. Intense transports are found in the region of a standing meander downstream of the southeast Indian Ridge, with weaker transports elsewhere. Averaged over the region (47°S-55.5°S and 135°E-155°E), the poleward heat transport by all transient processes in the model is 14.5±1.6 MW per meter of path length, poleward salt transport is not statistically different from zero (0.01 ± 0.01 m^2/s PSU per meter), and equatorward nitrate transport is 6.6 ± 0.7 mmol/s per meter.
3. long-lived, coherent mesoscale eddies in OFAM3-JRA55 contribute approximately 15-20% of the total poleward heat transport and equatorward nitrate transport

in our study region. The poleward salt transport by coherent eddies and all transient processes were of similar magnitude in the OFAM-JRA55 model, and not statistically different from zero in the Reynolds decomposition. This requires further investigation, as there was some offset of poleward salt transport by equatorward transports that would underestimate the poleward salt transport by all transient processes and increase the noise in the estimate.

4. the relationship between integrated surface elevation (ISE) and subsurface eddy content of heat, salt, and nitrate shows a statistically significant correlation and is consistent with the relationship found from one realisation of one cyclonic eddy sampled *in situ* observations. This result provides confidence in using ISE as a proxy to infer the total heat and salt content anomalies of coherent eddies in the absence of subsurface observations when first calibrated with *in situ* observations. Further investigation of methods to infer the nutrient content of an eddy from space is required because there may be seasonal and latitudinal dependence in the ISE proxy we derived for nitrate.

Our study demonstrates that *in situ* observations, although rare and expensive, provide a means to develop new proxy measures to greatly expand what we can learn from satellite observations about variability in the climate system. Extending this regional investigation to the circumpolar belt with a view to building the capability to remotely monitor meridional eddy fluxes of heat, salt, and nitrate is the focus of future work. Improved understanding and quantification of circumpolar fluxes are critical to understanding and predicting current and future variability in the Earth's energy balance, hydrological cycle and global ocean productivity.

Appendix A Eddy demography for south of Tasmania

Appendix B Algorithms to compute fluxes

B1 To compute transient fluxes

1. Obtained daily data of $v(x, y, z, t)$ and $T(x, y, z, t)$ or $S(x, y, z, t)$ or $N(x, y, z, t)$ over the period of 8 years from OFAM3-JRA55 and mapped them to the same grid points (velocity to tracer grid)
2. Computed mean over the record period: $\overline{v}(x, y, z)$ and $\overline{T}(x, y, z)$ or $\overline{S}(x, y, z)$ or $\overline{N}(x, y, z)$

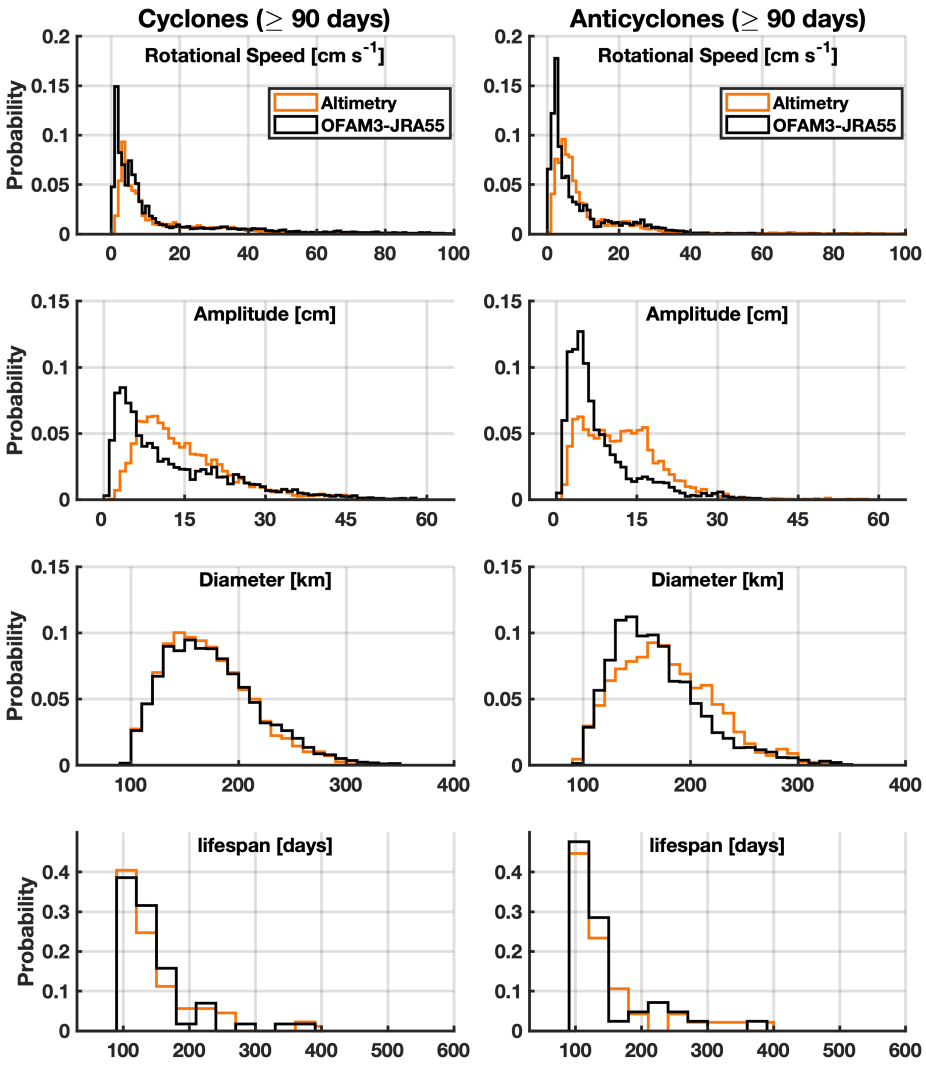

Figure A1. Histograms of rotational speed, amplitude, diameter, and lifespan of both cyclonic (left column) and anticyclonic (right column) eddies with a lifetime of at least 90 days. OFAM3-JRA55 results are in black, altimetry in orange.

3. Computed perturbations from the mean: $v'(x,y,z,t) = v(x,y,z,t) - \overline{v}(x,y,z)$, similarly for T', S' and N'
4. Computed the covariance of daily data as: $v'(x,y,z,t)T'(x,y,z,t)$, $v'(x,y,z,t)S'(x,y,z,t)$ and $v'(x,y,z,t)N'(x,y,z,t)$
5. Computed mean of the covariance: $\overline{v'T'}$ or $\overline{v'S'}$ or $\overline{v'N'}$

Table A1. Comparison of coherent eddies census between OFAM3-JRA55 and altimetry for the eddies that lived at least 90 days. Tabulated values are (min-max), mean ± standard deviation, and median ± IQR (Interquartile range).

	OFAM3-JRA55			Altimetry		
	Min – Max	Mean±Std	Median±IQR	Min – Max	Mean±Std	Median±IQR
Cyclonic eddies						
Amplitude (cm)	0.7-59.6	13.2±11	9.4±15	1.3-86.8	15.4±9.8	13±11.4
Diameter (km)	95.5-356.6	175.9±44.2	169.9±59.7	95.4-380.2	172.7±41.7	167.1±56.3
Lifespan (days)	92-369	146±58	130±54	90-584	164±101	126±73
Realisation		8300			14578	
Eddies		57			89	
Anticyclonic eddies						
Amplitude (cm)	0.6-38.5	8.1±6.7	5.8±6.8	0.8-57.7	12.4±7.5	11.7±10.1
Diameter (km)	95.3-352.8	169.1±43	161.6±54.2	95.3-443.8	178.7±46	173.3±63.4
Lifespan (days)	90-361	142±61	122±51	90-875	169±133	126±61
Realisation		5962			7922	
Eddies		42			47	

B2 To compute divergent eddy fluxes

1. Obtained daily data of $v(x, y, z, t)$ and $T(x, y, z, t)$ or $S(x, y, z, t)$ or $N(x, y, z, t)$ over the period of 8 years from OFAM3-JRA55 and mapped them to the same grid points (velocity to tracers grid)
2. The reference velocity is the near bottom velocity. So, we procured the deepest non-zero velocity in the water column $v_{ref}(x, y, t)$.
3. Projected $v_{ref}(x, y, t)$ on to all the valid depth levels as it would be $v_{ref}(x, y, z, t)$
4. Repeated the steps from 2 to 5, stipulated in the aforementioned section (B1), with $v_{ref}(x, y, z, t)$ in lieu of $v(x, y, z, t)$

Appendix C Coherent eddies' contribution to the total transient transport

We identified a total of 4987 realisations of 38 cyclonic and 1737 realisations of 18 anticyclonic eddies in the Subantarctic Zone (47°S-52°S and 135°E-155°E), regardless of their formation mechanism, over an 8-year study period. The total available tracer content carried by these eddies for each year is computed and presented in Table S5. On average, cyclonic eddies introduce anomalous heat content of $-0.4\pm0.05\times10^{20}$ J year^{-1}, salt content of $-1.52\pm0.24\times10^{12}$ kg year^{-1}, and nitrate content of $1.21\pm0.28\times10^{10}$ mol year^{-1} in the Subantarctic Zone. Likewise, anticyclonic eddies introduce anomalous heat content of $0.23\pm0.2\times10^{20}$ J year^{-1}, salt content of $1.01\pm0.81\times10^{12}$ kg year^{-1}, and nitrate content of $-0.53\pm0.67\times10^{10}$ mol year^{-1} in the region. Collectively, this constitutes net poleward transport of heat amounting to -0.1×10^{20} J year^{-1}, salt transport of -0.51×10^{12} kg year^{-1}, and equatorward transport of nitrate of 0.68×10^{10} mol year^{-1} by long-lived coherent eddies in the Subantarctic Zone south of Tasmania.

Table C1. Meridional transport of coherent mesoscale eddies and all transient processes in OFAM3-JRA55 over the Subantarctic Zone south of Tasmania (47°S-52°S and 135°E-155°E). The variability in the transport is computed as median absolute deviation over the region for transient processes. The standard deviation is used to describe the variability in the coherent eddies anomalies, computed over the mean annual anomalies (Table S5).

Transport	Heat (MW m^{-1})	Salt (m^2 s^{-1} PSU)	Nitrate (mmol m^{-1} s^{-1})
Transient processes	-11.7 ± 4.13	-0.15 ± 0.08	5.97 ± 2.25
Cyclonic eddies	-0.77 ± 0.12	-0.03 ± 0.005	0.27 ± 0.06
Anticyclonic eddies	0.51 ± 0.41	0.02 ± 0.02	-0.12 ± 0.15

Long-lived eddies carried -0.1×10^{20} J year^{-1} of heat poleward in the longitude band 135°E-155°E. This is equivalent to -0.26 MW m^{-1} (Table C1). The poleward transport of heat by all transient processes ($\overline{THF_d}$), in OFAM3-JRA55 averaged over the study region, was -11.7 MW m^{-1}. Therefore, coherent long-lived eddies accounted for approximately 2% of the transient heat transport south of Tasmania.

The salt content introduced by long-lived eddies in the 20° longitude band was -0.51×10^{12} kg year^{-1} in OFAM3-JRA55. This is equivalent to a poleward flux of -0.01 m^2 s^{-1} PSU. On the other hand, the average salt transport by all transient processes ($\overline{TSF_d}$) in OFAM3-JRA55 over the study region was -0.15 m^2 s^{-1} PSU. Therefore, the poleward salt transport attributed to long-lived eddies in our study region in this model is approximately 6% of the transient salt transport.

The nitrate anomaly carried by long-lived eddies in OFAM3-JRA55 was 0.68×10^{10} mol year^{-1} (Section 5.1). This is equivalent to equatorward transport of 0.15 mmol m^{-1} s^{-1}. The average nitrate transport by all transient processes ($\overline{TNF_d}$) in the model over the study region was 5.97 mmol m^{-1} s^{-1}. Thus, the equatorward nitrate transport attributed to the long-lived eddies in the region in this model is around 3% of the equatorward nitrate transport by all the transient processes.

Table C2. Meridional transport of coherent mesoscale eddies and all transient processes in OFAM3-JRA55 over the Subantarctic Front south of Tasmania (50°S-55.5°S and 135°E-155°E). The variability in the transport is computed as median absolute deviation over the region for transient processes. The standard deviation is used to describe the variability in the coherent eddies anomalies, computed over the mean annual anomalies (Table S6).

Transport	Heat (MW m^{-1})	Salt (m^2 s^{-1} PSU)	Nitrate (mmol m^{-1} s^{-1})
Transient processes	-22.1 ± 11.8	-0.14 ± 0.11	10 ± 5.05
Cyclonic eddies	-0.76 ± 0.15	-0.03 ± 0.006	0.19 ± 0.05
Anticyclonic eddies	0.82 ± 0.38	0.03 ± 0.01	-0.10 ± 0.09

Similar to the Subantarctic zone, the net tracer content carried by coherent eddies found in the Subantarctic Front is small compared to transient processes (Table C2 and S6). The small contribution of long-lived mesoscale eddies to the transient transport could be due to the compensating effect of cyclonic and anticyclonic eddies. The cyclonic eddies carried cold, fresh, and nitrate-rich waters, whereas the anticyclonic eddies carried warm, salty, and nitrate-depleted waters in both the Subantarctic Zone and Subantarctic Front region. Furthermore, the impact of eddies also varies geographically due to heterogeneous distribution of long-lived eddies in the study region. In OFAM3-JRA55, the

majority of the long-lived anticyclonic eddies are found upstream and over the South East Indian Ocean ridge, whereas the cyclonic eddies are found on downstream of the ridge possibly advecting tracers along and across the Subantarctic Front (Fig. S1).

Acknowledgments

This research was supported by Australian Research Council Discovery Projects (DP160102870), the Australian Research Council Special Research Initiative for Antarctic Gateway Partnership (SR140300001), and ship time from Australia's Marine National Facility (MNF).

R.P. thanks CSIRO-UTAS Quantitative Marine Science PhD program, Institute for Marine and Antarctic Studies, University of Tasmania, Hobart, Tasmania, Australia for financial support and the Australian Research Council Centre of Excellence for Climate Extremes for a thesis write-up scholarship. HP acknowledges funding from the Australian Government's National Environmental Science Program Earth Systems and Climate Change Hub and Climate Systems Science Hub and support from the Australian Research Council Centre of Excellence in Climate Extremes. RP thanks Prof. Nathan Bindoff for guidance to assess the stability of the transient fluxes. We thank two anonymous reviewers whose constructive comments greatly improved this manuscript.

The shipboard observations used in this study can be obtained either from the author's or MNF website (`https://www.cmar.csiro.au/data/trawler/survey_list.cfm?q=IN2016_V02`).

References

Abernathey, R., & Haller, G. (2018). Transport by lagrangian vortices in the eastern pacific. *Journal of Physical Oceanography*, *48*(3), 667–685.

Buzzicotti, M., Storer, B., Khatri, H., Griffies, S., & Aluie, H. (2023). Spatio-temporal coarse-graining decomposition of the global ocean geostrophic kinetic energy. *Journal of Advances in Modeling Earth Systems*, *15*(6), e2023MS003693.

Chelton, D. B., Schlax, M. G., & Samelson, R. M. (2011, October). Global observations of nonlinear mesoscale eddies. *Prog. Oceanogr.*, *91*(2), 167–216. doi: 10.1016/j.pocean.2011.01.002

Chelton, D. B., Schlax, M. G., Samelson, R. M., & de Szoeke, R. A. (2007, August). Global observations of large oceanic eddies. *Geophys. Res. Lett.*, *34*(15). doi: 10.1029/2007GL030812

Dawson, H. R., Strutton, P. G., & Gaube, P. (2018). The unusual surface chlorophyll signatures of Southern Ocean eddies. *Journal of Geophysical Research:*

Oceans, *123*(9), 6053–6069.

Dufour, C. O., Griffies, S. M., de Souza, G. F., Frenger, I., Morrison, A. K., Palter, J. B., ... others (2015). Role of mesoscale eddies in cross-frontal transport of heat and biogeochemical tracers in the Southern Ocean. *Journal of Physical Oceanography*, *45*(12), 3057–3081.

Faghmous, J. H., Frenger, I., Yao, Y., Warmka, R., Lindell, A., & Kumar, V. (2015). A daily global mesoscale ocean eddy dataset from satellite altimetry. *Scientific data*, *2*.

Foppert, A., Donohue, K. A., Watts, D. R., & Tracey, K. L. (2017). Eddy heat flux across the Antarctic Circumpolar Current estimated from sea surface height standard deviation. *Journal of Geophysical Research: Oceans*, *122*(8), 6947–6964. Retrieved from `http://dx.doi.org/10.1002/2017JC012837` doi: 10.1002/2017JC012837

Frenger, I., Muennich, M., Gruber, N., & Knutti, R. (2015, November). Southern Ocean eddy phenomenology. *J. Geophys. Res.-Oceans*, *120*(11), 7413–7449. doi: 10.1002/2015JC011047

Frenger, I., Münnich, M., & Gruber, N. (2018). Imprint of Southern Ocean eddies on chlorophyll. *Biogeosciences (BG)*, *15*, 4781–4798.

Griffies, S. M. (2014). Climate modeling with an energetic ocean mesoscale. *CLIVAR Exchanges*, *19*, 10–15.

Griffies, S. M., Schmidt, M., & Herzfeld, M. (2009). Elements of mom4p1. *GFDL Ocean Group Tech. Rep*, *6*, 377.

Hallberg, R. (2013). Using a resolution function to regulate parameterizations of oceanic mesoscale eddy effects. *Ocean Modelling*, *72*, 92–103.

Jayne, S. R., & Marotzke, J. (2002). The oceanic eddy heat transport. *Journal of Physical Oceanography*, *32*(12), 3328–3345.

Joyce, T., Patterson, S., & Millard, R. (1981). Anatomy of a cyclonic ring in the Drake Passage. *Deep Sea Research Part A. Oceanographic Research Papers*, *28*(11), 1265–1287.

Ladd, C., Mordy, C. W., Kachel, N. B., & Stabeno, P. J. (2007). Northern Gulf of Alaska eddies and associated anomalies. *Deep Sea Research Part I: Oceanographic Research Papers*, *54*(4), 487–509.

Langlais, C., Rintoul, S., & Schiller, A. (2011). Variability and mesoscale activity of

the southern ocean fronts: Identification of a circumpolar coordinate system. *Ocean Modelling*, *39*(1-2), 79–96.

Langlais, C., Schiller, A., & Oke, P. R. (2010). Southern ocean fronts in the bluelink reanalysis. *Mercator Quarterly Newsletter*, *36*, 50–57.

Marshall, J., & Shutts, G. (1981). A note on rotational and divergent eddy fluxes. *Journal of Physical Oceanography*, *11*(12), 1677–1680.

McGillicuddy Jr, D. J. (2016). Mechanisms of physical-biological-biogeochemical interaction at the oceanic mesoscale. *Annual Review of Marine Science*, *8*, 125–159.

Meijer, J. J., Phillips, H. E., Bindoff, N. L., Rintoul, S. R., & Foppert, A. (2022). Dynamics of a standing meander of the subantarctic front diagnosed from satellite altimetry and along-stream anomalies of temperature and salinity. *Journal of Physical Oceanography*, *52*(6), 1073–1089.

Meijers, A., Bindoff, N., & Roberts, J. (2007). On the total, mean, and eddy heat and freshwater transports in the Southern Hemisphere of a 1/8°× 1/8° global ocean model. *Journal of physical oceanography*, *37*(2), 277–295.

Moreau, S., Penna, A. D., Llort, J., Patel, R., Langlais, C., Boyd, P. W., ... others (2017). Eddy-induced carbon transport across the antarctic circumpolar current. *Global Biogeochemical Cycles*, *31*(9), 1368–1386.

Morrow, R., Coleman, R., Church, J., & Chelton, D. (1994). Surface eddy momentum flux and velocity variances in the Southern Ocean from Geosat altimetry. *Journal of Physical Oceanography*, *24*, 2050–2071.

Morrow, R., Donguy, J.-R., Chaigneau, A., & Rintoul, S. R. (2004). Cold-core anomalies at the Subantarctic front, south of Tasmania. *Deep Sea Research Part I: Oceanographic Research Papers*, *51*(11), 1417–1440.

Naveira Garabato, A. C., Ferrari, R., & Polzin, K. L. (2011). Eddy stirring in the southern ocean. *Journal of Geophysical Research: Oceans*, *116*(C9).

Nowlin Jr, W., Worley, S., & Whitworth III, T. (1985). Methods for making point estimates of eddy heat flux as applied to the Antarctic Circumpolar Current. *Journal of Geophysical Research: Oceans*, *90*(C2), 3305–3324.

Oke, P. R., Griffin, D. A., Schiller, A., Matear, R., Fiedler, R., Mansbridge, J., ... Ridgway, K. (2013). Evaluation of a near-global eddy-resolving ocean model. *Geoscientific model development*, *6*(3), 591.

Palter, J., Sarmiento, J. L., Gnanadesikan, A., Simeon, J., & Slater, R. (2010). Fueling export production: Nutrient return pathways from the deep ocean and their dependence on the Meridional Overturning Circulation. *Biogeosciences*, *7*(11), 3549–3568.

Patel, R. S., Llort, J., Strutton, P. G., Phillips, H. E., Moreau, S., Conde Pardo, P., & Lenton, A. (2020). The biogeochemical structure of southern ocean mesoscale eddies. *Journal of Geophysical Research: Oceans*, *125*(8), e2020JC016115.

Patel, R. S., Phillips, H. E., Strutton, P. G., Lenton, A., & Llort, J. (2019). Meridional heat and salt transport across the Subantarctic Front by cold-core eddies. *Journal of Geophysical Research: Oceans*, *124*(2), 981–1004.

Pegliasco, C., Chaigneau, A., & Morrow, R. (2015). Main eddy vertical structures observed in the four major Eastern Boundary Upwelling Systems. *Journal of Geophysical Research: Oceans*, *120*(9), 6008–6033.

Percival, D. B., Walden, A. T., et al. (1993). *Spectral analysis for physical applications*. cambridge university press.

Petersen, M. R., Williams, S. J., Maltrud, M. E., Hecht, M. W., & Hamann, B. (2013, April). A three-dimensional eddy census of a high-resolution global ocean simulation. *J. Geophys. Res.-Oceans*, *118*(4), 1759–1774. doi: 10.1002/jgrc.20155

Peterson, R., Nowlin Jr, W., & Whitworth III, T. (1982). Generation and evolution of a cyclonic ring at drake passage in early 1979. *Journal of Physical Oceanography*, *12*(7), 712–719.

Phillips, H. E., & Rintoul, S. R. (2000). Eddy variability and energetics from direct current measurements in the Antarctic Circumpolar Current south of Australia. *Journal of physical oceanography*, *30*(12), 3050–3076.

Pilo, G. S., Oke, P. R., Coleman, R., Rykova, T., & Ridgway, K. (2018). Patterns of vertical velocity induced by eddy distortion in an ocean model. *Journal of Geophysical Research: Oceans*, *123*(3), 2274–2292.

Rintoul, S. R. (2018). The global influence of localized dynamics in the Southern Ocean. *Nature*, *558*(7709), 209.

Rohr, T., Harrison, C., Long, M. C., Gaube, P., & Doney, S. C. (2020). The simulated biological response to southern ocean eddies via biological rate

modification and physical transport. *Global Biogeochemical Cycles*, *34*(6), e2019GB006385.

Sarmiento, J. L. (2013). *Ocean biogeochemical dynamics*. Princeton University Press.

Sekma, H., Park, Y.-H., & Vivier, F. (2013). Time-mean flow as the prevailing contribution to the poleward heat flux across the southern flank of the antarctic circumpolar current: A case study in the fawn trough, kerguelen plateau. *Journal of physical oceanography*, *43*(3), 583–601.

Su, Z., Wang, J., Klein, P., Thompson, A. F., & Menemenlis, D. (2018). Ocean submesoscales as a key component of the global heat budget. *Nature communications*, *9*(1), 1–8.

Swart, N. C., Ansorge, I. J., & Lutjeharms, J. R. (2008). Detailed characterization of a cold Antarctic eddy. *Journal of Geophysical Research: Oceans*, *113*(C1).

TheRingGroup. (1981). Gulf stream cold-core rings: Their physics, chemistry, and biology. *Science*, 1091–1100.

Thompson, A. F., & Naveira Garabato, A. C. (2014). Equilibration of the Antarctic Circumpolar Current by standing meanders. *Journal of Physical Oceanography*, *44*(7), 1811–1828.

Thompson, A. F., & Sallée, J.-B. (2012). Jets and topography: Jet transitions and the impact on transport in the Antarctic Circumpolar Current. *Journal of physical Oceanography*, *42*(6), 956–972.

Tréguier, A.-M., Deshayes, J., Le Sommer, J., Lique, C., Madec, G., Penduff, T., ... Talandier, C. (2014). Meridional transport of salt in the global ocean from an eddy-resolving model. *Ocean Science*, *10*(2), 243–255.

Tréguier, A.-M., Lique, C., Deshayes, J., & Molines, J.-M. (2017). The north atlantic eddy heat transport and its relation with the vertical tilting of the gulf stream axis. *Journal of Physical Oceanography*, *47*(6), 1281–1289.

van Ballegooyen, R. C., Gründlingh, M. L., & Lutjeharms, J. R. (1994). Eddy fluxes of heat and salt from the southwest indian ocean into the southeast atlantic ocean: A case study. *Journal of Geophysical Research: Oceans*, *99*(C7), 14053–14070.

Watts, D. R., Sun, C., & Rintoul, S. (2001). A two-dimensional gravest empirical mode determined from hydrographic observations in the Subantarctic front.

Journal of Physical Oceanography, *31*(8), 2186–2209.

Watts, D. R., Tracey, K. L., Donohue, K. A., & Chereskin, T. K. (2016). Estimates of Eddy Heat Flux Crossing the Antarctic Circumpolar Current from Observations in Drake Passage. *Journal of Physical Oceanography*, *46*(7), 2103–2122.

Zhang, X., Oke, P., Feng, M., Chamberlain, M., Church, J., Monselesan, D., ... Fiedler, R. (2016). A near-global eddy-resolving ogcm for climate studies. *Geosci. Model Dev. Discuss*, *2016*, 1–52.